

RXTE OBSERVATION OF CYGNUS X-1: II. TIMING ANALYSIS,

MICHAEL A. NOWAK¹, BRIAN A. VAUGHAN², JÖRN WILMS³, JAMES B. DOVE^{1,4,5}, MITCHELL C. BEGELMAN^{1,5}*Submitted to The Astrophysical Journal, April 3, 1998*

ABSTRACT

We present timing analysis for a Rossi X-ray Timing Explorer observation of Cygnus X-1 in its hard/low state. This was the first RXTE observation of Cyg X-1 taken after it transited back to this state from its soft/high state. RXTE's large effective area, superior timing capabilities, and ability to obtain long, uninterrupted observations have allowed us to obtain measurements of the power spectral density (PSD), coherence function, and Fourier time lags to a decade lower in frequency and half a decade higher in frequency than typically was achieved with previous instruments. Notable aspects of our observations include a weak 0.005 Hz feature in the PSD coincident with a coherence recovery; a 'hardening' of the high-frequency PSD with increasing energy; a broad frequency range measurement of the coherence function, revealing rollovers from unity coherence at both low and high frequency; and an accurate determination of the Fourier time lags over two and a half decades in frequency. As has been noted in previous similar observations, the time delay is approximately proportional to $f^{-0.7}$, and at a fixed Fourier frequency the time delay of the hard X-rays compared to the softest energy channel tends to increase logarithmically with energy. Curiously, the 0.01–0.2 Hz coherence between the highest and lowest energy bands is actually slightly greater than the coherence between the second highest and lowest energy bands. We carefully describe all of the analysis techniques used in this paper, and we make comparisons of the data to general theoretical expectations. In a companion paper, we make specific comparisons to a Compton corona model that we have successfully used to describe the energy spectral data from this observation.

Subject headings: accretion — black hole physics — X-rays: binaries

1. INTRODUCTION

1.1. *Plan of Paper*

Recently, we have presented the results of a spectral analysis of a 20 ks Rossi X-ray Timing Explorer (RXTE) observation of perhaps the most famous of the galactic black hole candidates (GBHC), Cygnus X-1 (Dove et al. 1998, hereafter paper I). The results of this analysis are summarized in §1.3 below. Here in this paper we focus on the timing analysis of our RXTE observation. Specifically, we present the Cyg X-1 power spectral density (PSD), the coherence function, and the time delays between soft and hard lightcurve variability. We discuss in general terms the analysis techniques that we have used. As the cross-spectral techniques utilized for determining time lags and coherence are unfamiliar to many researchers, we shall adopt a somewhat "pedagogical tone" at times. Practitioners in the field themselves have not always properly defined error bars and noise limits (cf. §3.1, §4.2). Cross spectral techniques are used increasingly in the study of X-ray binaries, and they have benefits relative to the more conventional cross correlation function, particularly in measurements with large signal-to-noise (S/N). We hope that the discussion here is of general use.

We begin this paper with a review of the parameters of the Cygnus X-1/HDE 226868 system in general (section 1.2), and the modeling of the Cyg X-1 high energy spectrum in specific (section 1.3). The rest of the paper is devoted to studying the variability of our RXTE Cyg X-1 data. In section 2 we define the periodogram for *one* lightcurve, i.e. the PSD, and describe

how to account for instrumental effects. We present our results for Cyg X-1 in five different energy bands. Comparing the lightcurves measured simultaneously in these different energy bands can reveal further information on the nature of the underlying physical processes. Section 3 describes our computations of the coherence function, while section 4 describes our measurements of the time delay between the variability components of different energy bands. Coherence measures the degree of linear correlation between time series as a function of time scale, or equivalently of Fourier frequency. In both of these sections, we illustrate the techniques, estimates of noise levels, etc., with our RXTE data for Cyg X-1. More importantly, we apply the techniques to the Cyg X-1 data in order to help constrain physical models of this system. In section 5 we interpret our Cyg X-1 results in terms of simple, physical toy models. Specific results and comparisons for the Comptonization model of paper I are presented in a companion paper (Nowak et al. 1998, hereafter paper III).

1.2. *Parameters of the Cygnus X-1/HDE 226868 System*

Cygnus X-1 is one of the most firmly established persistent GBHC. Discovered in a rocket flight in 1964 (Bowyer et al. 1965), this object was one of the first X-ray sources known, although its exact nature was not clear until its optical identification with the O-star HDE 226868 (Hjellming 1973). Since then, Cyg X-1 has been the subject of observations by almost all X-ray astronomy missions. In-depth reviews have been published by Oda (1977) and Liang & Nolan (1984). Table 1 lists

¹JILA, University of Colorado, Campus Box 440, Boulder, CO 80309-0440, USA; {mnnowak, dove}@rocinante.colorado.edu, mitch@jila.colorado.edu²Space Radiation Laboratory, California Institute of Technology, MC 220-47, Pasadena, CA 91125, USA; brian@srl.caltech.edu³Institut für Astronomie und Astrophysik, Abt. Astronomie, Waldhäuser Str. 64, D-72076 Tübingen, Germany; wilms@astro.uni-tuebingen.de⁴also, Department of Physics and Astronomy, University of Wyoming, Laramie, WY 82071, USA⁵also, Department of Astrophysical and Planetary Sciences, University of Colorado, Boulder, CO 80309, USA

the most important parameters of the system.

The black hole mass given in Table 1 is lower than the usually quoted value of $16 \pm 5 M_{\odot}$ determined by Gies & Bolton (1986). These authors determined the mass by using a relationship between the rotational broadening of the absorption lines of HDE 226868 and the radial velocity, and by assuming that these two values depend only on the mass ratio. By modeling the light curve they found $M = 33 \pm 9 M_{\odot}$ for HDE 226868. The black hole mass of $16 M_{\odot}$ was then determined using the mass function given in Table 1. This fairly high value has propagated into the literature, and is quoted in most reviews on black holes (e.g., Tanaka & Lewin 1995). It should be noted, however, that the method used by Gies & Bolton (1986) is nonstandard, and that their mass estimate for HDE 226868 disagrees with those obtained by other methods. Masses obtained from photometric modulations are in the range of $16 \pm 2 M_{\odot}$ for HDE 226868 and $8 \pm 3 M_{\odot}$ for the black hole (Balog, Goncharski & Cherepashchuk 1981; Hutchings 1978). Masses following from a determination of the $\log g$ value of the O-star atmosphere typically result in masses of around $15 M_{\odot}$ for HDE 226868 (Herrero et al.

For our purposes, the main parameters of interest in Table 1 are the compact object mass, system luminosity, and system distance. However, few reviews have included all the potential parameters of interest. Furthermore, many reviews quote secondary sources. For these reasons, we present Table 1.

1.3. Spectral Results

The X-ray spectrum of Cyg X-1 and other galactic black hole candidates in the hard state can be represented as the sum of a soft thermal component and a hard, non-thermal, power law component with a high energy cutoff at about 150 keV. The spectrum is further modified by reprocessing features, in particular a weak iron fluorescence line at 6.4 keV and possibly a Compton reflection hump at energies around 30 keV. All four components are usually explained in the context of accretion disk corona models (Hua & Titarchuk 1995; Svensson & Zdziarski 1994; Coppi 1992; Sunyaev & Titarchuk 1980; Sunyaev & Trümper 1979). These models assume that the thermal radiation originates in an accretion disk and is Comptonized in a hot plasma, the “accretion disk corona” (ADC). Comptonization results in a non-thermal power-law spectrum. The iron line and the reflection hump suggest that part of the hard radiation from the ADC is reprocessed by the comparatively cold (150 eV) accretion disk.

The exact geometrical configuration of the accretion disk and the corona is unknown, and is one of the major subjects of black hole X-ray astronomical research. Due to the similarity between the hard state X-ray spectrum of galactic black hole candidates and active galactic nuclei (AGN), most previous work has assumed a “sandwich configuration” where the corona is situated above and below the accretion disk (Poutanen, Svensson & Stern 1997; Hua & Titarchuk 1995; Haardt & Maraschi 1993 and references therein). The evidence for a sandwich configuration in GBHC, however, is not as strong as in the case of AGN. In previous work, some of us have pointed out that the efficiency of Compton cooling might prevent the sandwich corona from getting hot enough to generate the hard X-ray spectrum observed in the hard state of Cyg X-1 (Dove, Wilms & Begelman 1997; Wilms et al. 1997; Gierliński et al. 1997; Poutanen, Krolik & Ryde 1997). Due to the high geo-

1995; Sokolov 1987; Aab et al. 1984, and references therein). Since the work by Herrero et al. (1995) represents the “state of the art” in the theory of hot stellar atmospheres including wind loss, we present their value for the mass of HDE 226868. We consequently use a smaller black hole mass in this paper. This mass is still high enough, however, to point without doubt to the presence of a black hole in the system.

A problem intimately connected with estimating the black hole mass is the determination of the orbital inclination. The value of 35° in Table 1 is presented without a statement of its uncertainty. Inclination measurements are intrinsically imprecise because the inclination has to be determined from difficult optical polarization measurements and consequently the values found for the inclination are scattered from 26° to 67° (Bochkarev et al. 1986; Ninkov, Walker & Yang 1987a; Ninkov, Walker & Yang 1987b; Dolan 1992, and references therein) with most authors deriving rather lower inclinations. For these reasons we use $i = 35^{\circ}$, the value adopted by Herrero et al. (1995) in their mass determination shown in Table 1.

metrical covering factor of the corona, about 50 per cent of all hard radiation from the corona enters the cold accretion disk, where it is either reflected or thermalized. The soft photons produced this way again enter the corona where they efficiently Compton cool the plasma. For a given Thomson optical depth of the corona, there thus exists a maximum coronal temperature above which no self consistent solutions exist.

Since the major physical cause preventing the sandwich configuration from explaining the observed hard spectra is the very efficient Compton cooling, we have sought alternative geometries that do not suffer from a large covering factor. The need for a smaller covering factor is also seen from the weakness of the reflection features in GBHC compared to those in AGN. In our previous work we have advocated one such configuration, the “sphere+disk” geometry (Dove et al. 1997, see also Gierliński et al. 1997; Poutanen, Krolik & Ryde 1997). Here, a hot spherical corona surrounds the black hole, while the cold accretion disk which provides the seed photons is situated farther outside. This geometry obviously has a smaller covering factor, and in fact much higher coronal temperatures are possible (Dove et al. 1997). Using self consistent numerical models computed for the sphere+disk geometry we were able to describe successfully the hard-state spectrum of Cyg X-1 measured by RXTE over a broad range in energy, 3–200 keV (Dove et al. 1997; paper I). We derived an optical depth for the spherical corona of $\tau = 1.6 \pm 0.1$ and an average temperature of $kT = 87 \pm 5$ keV (paper I).

To facilitate comparison with previous work, and to test for the presence of features in the broad-band spectrum, we also performed purely phenomenological fits to Cyg X-1. We found that the 3 to 200 keV RXTE spectrum could be described by an exponentially cut-off power law with a photon index $\Gamma = 1.45^{+0.01}_{-0.02}$, e-folding energy $E_f = 162^{+9}_{-8}$ keV, plus a deviation from a power law that formally can be modeled as a thermal blackbody with temperature $kT_{bb} = 1.2^{+0.0}_{-0.1}$ keV. Note that the above power law index is harder than that typically found, which might be an indication that the source was not in its usual “hard state” after exiting the “soft state” of 1996 (Cui et al. 1997a; Zhang et al. 1997 and references therein), which ended only a few weeks prior to our observation. No hardening was

Table 1: Parameters for the system Cyg X-1/HDE 226868. Values in parentheses are uncertainties in units of the last digit.

	Optical Companion HDE 226868	Compact Object Cyg X-1	System Parameters	References
Position:				
J2000.0:	α		$19^{\text{h}}58^{\text{m}}21.^{\text{s}}700$	1
	δ		$+35^{\circ}12'05.^{\text{s}}82$	1
galactic:	l_{II}		$71^{\circ}33$	1
	b_{II}		$+3^{\circ}07$	1
Spectral Type	O9.7 Iab			2
T_{eff} [K]	32 000			3
$E_{\text{B-V}}$	0.95(7)			4
N_{H} [cm $^{-2}$]			$6(2) \times 10^{21}$	4,5
Distance [kpc]			$2.5(3)$	6
m_{V} [mag]	8.84			7
B_{T} [mag]	9.828(22)			7
V_{T} [mag]	9.020(17)			7
B – V [mag]	+0.81			8
U – B [mag]	-0.28			8
Luminosity [L_{\odot}]	$10^{5.4}$	10^4		3,9
Luminosity [erg/s]	10^{39}	$4 \cdot 10^{37}$		
Inclination			35°	10
$a \sin i$ [km]		$5.82(8) \times 10^6$		11
Orbital Period [d]			$5.59974(8)$	11
Major Axis [R_{\odot}]	14.6	26.3		10
$v \sin i$ [km/s]	75.6(10)			11
Mass Function [M_{\odot}]	0.252(10)			11
Mass [M_{\odot}]	18	10		10
Radius	$17 R_{\odot}$	30 km^{\dagger}		3
Separation [R_{\odot}]			41	10
Mass loss rate [M_{\odot}/a]			3×10^{-6}	3
Wind velocity [km/s]	2100			10

¹Turon et al. (1992), ²Walborn (1973), ³Herrero et al. (1995), ⁴Wu et al. (1982), ⁵Bałucińska-Church et al. (1995), ⁶Ninkov, Walker & Yang (1987b), ⁷ESA (1997), Volume 9, ⁸Lutz & Lutz (1972), ⁹Liang & Nolan (1984), ¹⁰see text for further explanation, ¹¹Gies & Bolton (1982)

[†] Schwarzschild radius

Table prepared in collaboration with Katja Pottschmidt (Pottschmidt 1997).

seen in the HEXTE data from 30 to 100 keV, indicating that any reflection features were formally very weak. [That is, the presence of reflection needs to be inferred from more sophisticated continuum models (Dove et al. 1998; Gierliński et al. 1997; Poutanen, Krolik & Ryde 1997), rather than from simple exponentially cutoff power laws reflected from cold slabs.]

2. POWER SPECTRAL DENSITY

2.1. Techniques and Noise Levels

The RXTE observations presented here were performed October, 22, 1996. For the timing analysis we used data obtained with the Proportional Counter Array (PCA), the low energy instrument onboard RXTE. The PCA consists of five nearly identical Xe proportional counters units (PCU) with a total effective area of about 6500 cm^2 (Jahoda et al. 1996). The data extraction was performed using the RXTE standard data analysis software, ftools 4.0. To avoid contamination of the data due to the Earth's X-ray bright limb, only data measured at source elevations more than 10° above the spacecraft horizon were used.

As discussed in paper I, throughout our observations Cyg X-1 showed count rates of $\approx 4300 \text{ cts s}^{-1}$. The total integrated on source time for our observation was slightly more than 20 ks. For approximately 2 ks two PCU of the PCA were not operational, so these data were ignored. We therefore had approximately 18 ks of high quality timing data¹. The PCA data modes for our observation are listed in Table 2, the formal characteristics of the modes can be found in Appendix F to the NASA Research Announcement for RXTE (NASA 1997).

We divided our data into 5 energy bands with $\mathcal{O}(700-1000 \text{ cts s}^{-1})$ each, binned at 2^{-9} s resolution². We also created a very high energy band which our energy spectral analysis indicated should be entirely dominated by background counts. This was done to assess the level at which background fluctuations could affect our results at lower energies. Thus, we created lightcurves for six energy bands in all, labeled 1–6. The properties of these energy channels are listed in Table 3.

We calculated Power Spectral Densities (PSD) in each channel by dividing the data into contiguous segments of uniform length and time resolution, and performing a Fast Fourier Transform (FFT) on each data segment. (Segments with data gaps of *any* duration were ignored.) We performed all the FFTs using the reverse discrete transform from IDL (Version 4.0.1), which corresponds to

$$S_j \equiv \sum_{k=0}^{N-1} s_k \exp(2\pi i j k / N) . \quad (1)$$

Here s_k is the counts in the k^{th} bin of the lightcurve (consisting of N evenly spaced time bins), and S_j is the complex discrete Fourier transform corresponding to the Fourier frequency $f_j = j/N T_s^{-1}$, where T_s is the length (in seconds) of each data segment and $j \in [-N/2, N/2]$. From S_j , we form the discrete

PSD,

$$\langle |S_j|^2 \rangle = \langle S_j^* S_j \rangle , \quad (2)$$

where the angle brackets indicate an average over data segments *and*, in most cases, over frequency bins. Throughout we have used a logarithmic frequency binning wherein we averaged over frequencies $f \rightarrow f + df$, with $df/f = 0.15$.

We have employed the PSD normalization of Miyamoto et al. (1991). In this normalization, one multiplies $\langle |S_j|^2 \rangle$ by $2\mathcal{R}^{-2}T^{-1}$, where \mathcal{R} is the mean count rate (in cts s^{-1}) for the energy band of interest. As $|S_j|^2 = |S_{-j}|^2$, we have adopted a ‘one sided’ normalization. The factor of 2 in the definition of the PSD is introduced so that integrating the PSD over positive Fourier frequencies and then taking the square root yields the normalized root mean square (rms) variability

$$\text{rms} = \left(\frac{\langle s^2 \rangle - \langle s \rangle^2}{\langle s \rangle^2} \right)^{1/2} , \quad (3)$$

where here the average is over individual data segments and time bins. Note that rms variability is often quoted for the PSD integrated over restricted frequency ranges. We shall always explicitly state the frequency ranges used in our measurements. Throughout the rest of the paper we shall take $P_s(f_j) = 2\mathcal{R}^{-2}T^{-1}|S(f_j)|^2$ to signify a PSD as calculated from a discrete FFT. When considering two energy channels, P_s will indicate the PSD of the soft channel, and P_h the PSD of the hard channel.

To leading order (cf. Leahy et al. 1983; van der Klis 1989), counting noise leads to an additive “white noise” component. Its PSD, which we write $P_N(f)$, has an amplitude of $2/\mathcal{R}$, independent of Fourier frequency. Its error is $\mathcal{O}(1)$ for a *single* Fourier frequency measured from a *single* data segment, and is distributed as $1/\mathcal{R}$ times χ^2 with 2 degrees of freedom³. Instrumental deadtime (cf. Zhang et al. 1995) modifies this slightly. By deadtime we mean any process where the detection of an event subsequently changes the sensitivity of the detectors [see Zhang et al. (1995); Zhang & Jahoda (1996) for a discussion of idealized models that can be used to approximate the effects seen in RXTE data]. Here we use the deadtime model of Zhang et al. (1995), as was successfully applied by Morgan, Remillard & Greiner (1997) to RXTE data of GRS 1915+105. The expectation value for the PSD of the noise level is different for each energy band, and is given by

$$\begin{aligned} P_N(f) = & \frac{2}{\mathcal{R}_e} \left(\left[1 - 2\mathcal{R}_{pe}\tau_d \left(1 - \frac{\tau_d}{2t_b} \right) \right] \right. \\ & - \frac{N_f - 1}{N_f} \mathcal{R}_{pe}\tau_d \left(\frac{\tau_d}{t_b} \right) \cos(2\pi t_b f) \\ & \left. + \mathcal{R}_{pe}\mathcal{R}_{vle} \left[\frac{\sin(\pi\tau_{vle}f)}{\pi f} \right]^2 \right) , \end{aligned} \quad (4)$$

¹Note that this is slightly less than twice the duration of the observations we used for the spectral analysis of paper I. Approximately half the *standard2f* data were not included in the first data tape that we received; however, all the timing data were included.

²We also created lightcurves from one quarter of our 2^{-12} s resolution data to search for high-frequency signatures. No variability in excess of counting noise was observed above $\approx 200 \text{ Hz}$. We therefore chose to perform our analyses with 2^{-9} s resolution data.

³The fractional uncertainty in the signal component of the PSD is also of $\mathcal{O}(1)$, as measured for an individual Fourier frequency from the FFT of a single data segment (cf. Bendat & Piersol 1986; van der Klis 1989).

where \mathcal{R}_e is the total count rate in the energy band of interest, \mathcal{R}_{pe} is the count rate *per PCU* in the energy band of interest (as all five PCU were always on for our selected observations, $\mathcal{R}_{pe} = \mathcal{R}_e/5$), \mathcal{R}_{vle} is the ‘very large event rate’ (mainly due to high energy charged particles, and $< 100 \text{ cts s}^{-1}$), τ_d is the detector deadtime (for the PCA we take $\tau_d = 10 \mu\text{s}$; W. Zhang, Private Communication), τ_{vle} is the deadtime for very large events (preset to $70 \mu\text{s}$ for our observation), N_f is the number of frequency bins in the FFTs ($N_f = N/2$), and t_b is the duration of the time bins in the input lightcurves. In practice, the terms involving the cosine and sine above are negligible for the count rates and frequencies of interest to us. The above formula was compared to the 600–2048Hz PSDs calculated from our single bit data. Assuming that those frequencies were entirely dominated by counting noise modified by deadtime effects, eq. (4) was accurate to better than $2 \times 10^{-3}/\mathcal{R}_e$ (absolute). Thus eq. (4) correctly predicts the deadtime *deviation* from the uncorrected noise level of $2/\mathcal{R}_e$ to better than 25%.

We use eq. (4) throughout this work to estimate the deadtime-corrected Poisson noise level. All averaged PSD we present have had this level subtracted off, as have all quoted rms variability levels. The uncertainty in the mean of the PSD is computed by dividing the *uncorrected* mean PSD by the square root of the total number of independent segments and/or frequency bins averaged together (cf. Leahy et al. 1983; van der Klis 1989). The *minimum* mean PSD level detectable with our observations is approximately the counting noise level from eq. (4) divided by the square root of the number of data segments and/or frequency bins averaged over. We explicitly show this ‘effective noise level’ for all of our average PSDs. The logarithmic binning in frequency results in an approximately $f^{-0.5}$ dependence for the effective noise level at high frequency. In the next section, we describe our results for Cyg X-1.

2.2. Results for Cygnus X-1

We performed FFTs with three data segment lengths: 1024s (10 data segments), 128s (133 data segments), and 32s (556

data segments). In Figure 1 we show PSDs calculated from these FFTs. As the PSDs for each segmentation of the data are statistically correlated, the frequency range 9.7×10^{-4} – 1.3×10^{-2} Hz is computed from the 1024s data segments, the frequency range 7.8×10^{-3} – 5.9×10^{-2} Hz is computed from the 128s data segments, and the frequency range 3.1×10^{-2} – 256 Hz is computed from the 32s data segments. We use the exact same data for calculating the coherence function and time lags described below.

The RXTE deadtime is energy dependent (Zhang & Jahoda 1996), and in fact the PSD for the background dominated, (45–100 keV) band is above the effective noise level. Either eq. (4) is inadequate or part of the PSD in this channel may be caused by variability of the background or source. However, if the $10 \mu\text{s}$ deadtime estimation truly is good to better than $\approx 25\%$ at low energy, then our noise-subtracted PSDs are reliable to at least 100 Hz.

For all energy bands, the rms variability in the 10⁻³–100 Hz frequency range is $\approx 30\%$. The PSDs are relatively flat from 0.02–0.2 Hz, then fall off at higher frequencies. A portion of the higher frequency range has an f^{-1} dependence. This behavior is characteristic of the low state of BHC in general (Belloni & Hasinger 1990a; Belloni & Hasinger 1990b; Miyamoto et al. 1992). There is evidence that the PSD steepens again at frequencies below 3×10^{-3} Hz, especially in the lower energy bands. This low frequency noise is partly responsible for the greater total rms in the lower energy bands. Low frequency noise reported previously has been studied by Pottschmidt et al. (1998) and Angelini, White & Stella (1994). There also is a weak bump, seen in all energy bands, in at least two frequency bins near 0.005 Hz. The rms variability of this region in each PSD is $\approx 1.5\%$. This feature taken on its own is too weak to be called a quasi-periodic oscillation (QPO). A Lomb-Scargle periodogram (Lomb 1976; Scargle 1982) of the entire data set also shows this feature; however, its significance is only 50–85%. (The significance is greatest in the lowest energy band.) As we shall discuss in §3 below, however, this region of the PSD, un-

Table 2: Data modes, with their energy ranges, number of energy channels, and time resolution (always constrained to be a power of 2 s by the onboard data processors), for our Cyg X-1 observation.

Data Mode	Energy Range (keV)	No. Chan.	Time Res. (s)
B_2ms_8B_0_35_Q	0–14.1	8	2^{-9}
SB_250us_0_13_2s	0–5	1	2^{-12}
SB_250us_14_35_2s	5–14.1	1	2^{-12}
E_125us_64M_36_1s	14.1–100	64	2^{-13}

Table 3: The energy bands used in this work (labeled 1–6). Also listed are the corresponding PHA channels, their approximate energy range, the mean energy of the energy band for our specific observations, and the average count rate in the band.

Energy Band	PHA Chan.	Energy Range (keV)	Mean Energy (keV)	Mean Count Rate (cts s ⁻¹)
1	0–10	0–3.9	2.5	780
2	11–16	3.9–6.0	4.8	1040
3	17–22	6.0–8.2	7.1	730
4	23–35	8.2–14.1	10.4	890
5	36–193	14.1–45	20.1	780
6 [†]	194–255	45–100		70

[†] Dominated by background counts. Not used for analysis. Background accounts for $\approx 1\%$ of the counts in band 1, up to $\approx 8\%$ of the counts in band 5. Therefore, none of the conclusions in this paper should be strongly influenced by the background.

like the surrounding frequency bins, has near unity coherence. Low frequency ‘peaks’ in the Cyg X-1 PSD previously have been observed at frequencies ranging from 0.04–0.07 Hz (Angelini & White 1992; Kouveliotou et al. 1992; Angelini, White & Stella 1994; Ubertini et al. 1994; Vikhlinin et al. 1994). For the most part these features did not appear as broad peaks with a Lorentzian profile. Rather, they appeared as regions in the PSD where the power law slope, as a function of Fourier frequency, discontinuously changed from positive to negative. Furthermore, previous observations did not consider the coherence of these low frequency features between different energy bands.

As a phenomenological description of the PSDs, we have fit doubly broken power laws over the frequency range 0.02–90 Hz. We show an example of one of these fits in Figure 2. The reduced χ^2 for these fits ranged from 4 for the lowest energy channel to 16 for the highest energy channel. The somewhat large reduced χ^2 values result from the excellent statistics of the data, and indicate that doubly broken power laws are only qualitative fits to the PSDs. Although the PSD definitely contain structure not fit by the broken power law, Figure 2 shows that they capture the essential features of the 0.02–90 Hz data. The overall normalization of the fits decreases slightly with increasing energy. The low-frequency power-law index, the middle-frequency power-law index, and the two energy breaks do not show any significant dependence upon channel energy. The high frequency power law index, on the other hand, clearly ‘hardens’ with increasing energy. This hardening of the PSD with increasing energy is evident in Figure 2b. We present all of our best fit parameter values in Table 4.

The results of this doubly broken power law fit are comparable to the results found by Belloni & Hasinger (1990a) using multiple EXOSAT observations. These authors also found the PSD to be flat below a break at 0.04–0.4 Hz, then approximately $\propto f^{-1}$ up to a break at 1–6 Hz, and approximately $\propto f^{-2}$ at higher frequencies. There was weak evidence for the high frequency power law becoming less steep with increasing energy as seen here. Furthermore, the overall rms variability ranged from 28%–38%, consistent with the values discussed here. Our results and those of Belloni & Hasinger (1990a) are also consistent with the trends observed by *Ginga*, as shown in Miyamoto et al. (1992). Belloni & Hasinger (1990a), however, did not consider the coherence or time delays between various energy bands. As we shall discuss below, these additional statistics offer the promise of constraining physical models of this system.

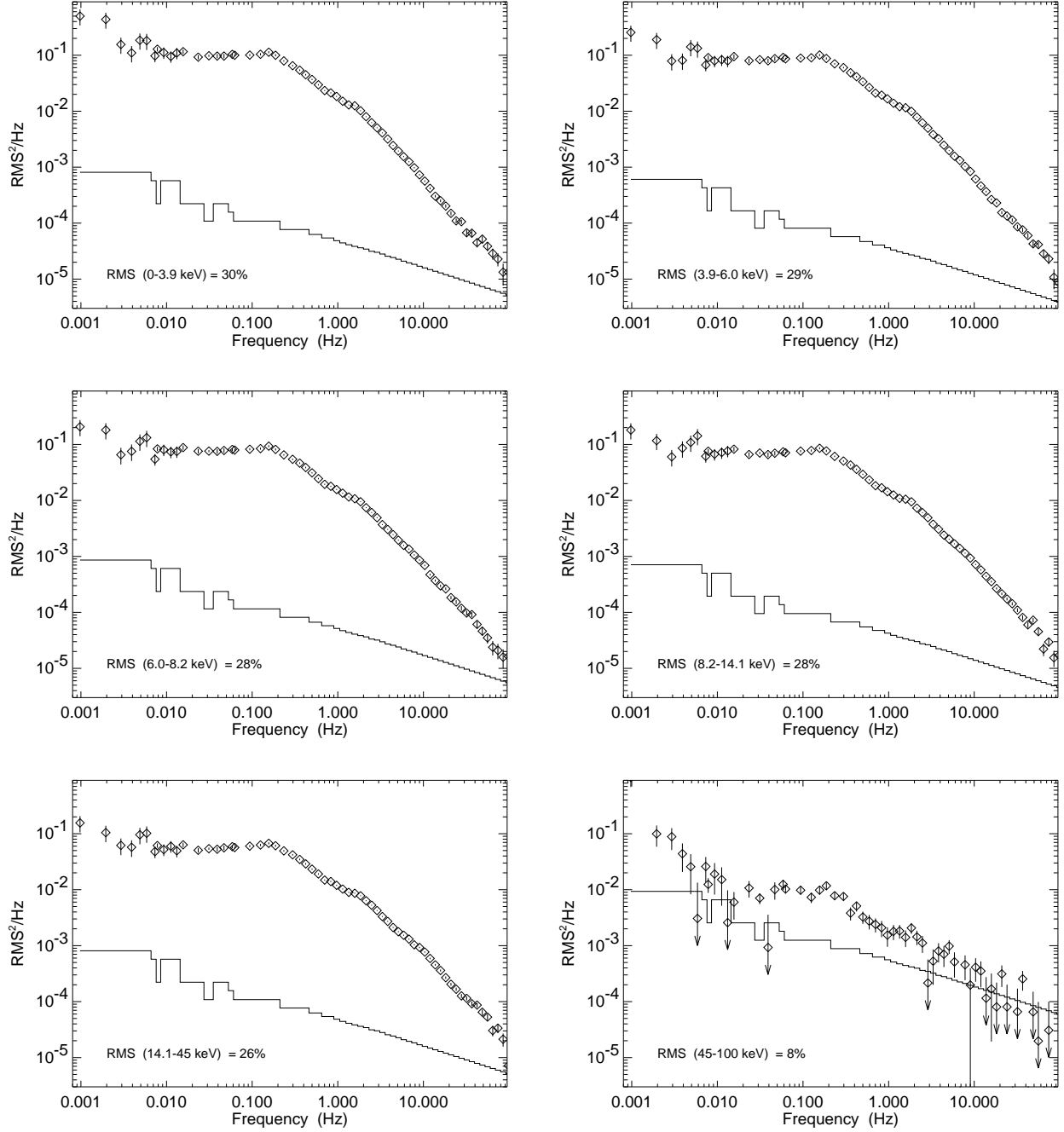


Fig. 1.— Noise-subtracted mean Power Spectral Densities (PSD) for the five energy bands (and one ‘background’ band, see text) considered in this work. *Top left:* (0–3.9 keV). *Top right:* (3.9–6.0 keV). *Middle left:* (6.0–8.2 keV). *Middle right:* (8.2–14.1 keV). *Bottom left:* (14.1–45 keV). *Bottom right:* (45–100 keV). For all PSDs, diamonds represent the average PSD with a normalization such that the square root of the integrated PSD is the fractional root mean square (rms) variability (see text and Miyamoto et al. 1991). The solid line represents the “effective noise” level, which is essentially the minimum level of variability that could have been detected with our observations. All quoted rms variability levels are for the frequency range 9.7×10^{-4} –100 Hz, except for the (45–100 keV) band which is the 9.7×10^{-4} –10 Hz range.

Table 4: Parameter values for a doubly broken power law fit to the 0.02–90 Hz PSD data. The lowest frequency PSD is fit to a function of the form $A_n f^{\alpha_1}$. The location of the first break is at β_1 and α_2 is the best fit index of the second power law. The location of the second break is at β_2 and α_3 is the best fit index of the third power law. The reduced χ^2_r values for all the fits are for 44 degrees of freedom. Uncertainties given are at the 90% level for one interesting parameter ($\Delta\chi^2 = 2.7$). Parameters without errors have uncertainties smaller than the last shown decimal place.

Channel Energy	A_n	α_1	β_1 [Hz]	α_2	β_2 [Hz]	α_3	χ^2_r
(0–3.9 keV)	0.124 ± 0.001	$0.090^{+0.005}_{-0.000}$	0.17	$-0.994^{+0.001}_{-0.006}$	2.1	$-1.67^{+0.00}_{-0.07}$	4.0
(3.9–6.0 keV)	0.116 ± 0.001	$0.094^{+0.008}_{-0.002}$	0.17	-0.970 ± 0.003	$2.1^{+0.5}_{-0.0}$	$-1.68^{+0.08}_{-0.0}$	6.1
(6.0–8.2 keV)	$0.130^{+0.005}_{-0.027}$	$0.092^{+0.000}_{-0.012}$	0.17 ± 0.01	$-0.970^{+0.053}_{-0.003}$	$2.2^{+0.6}_{-0.1}$	$-1.61^{+0.04}_{-0.00}$	4.4
(8.2–14.1 keV)	$0.093^{+0.003}_{-0.000}$	$0.092^{+0.000}_{-0.011}$	0.19 ± 0.01	$-0.985^{+0.054}_{-0.000}$	$2.1^{+0.5}_{-0.1}$	$-1.48^{+0.03}_{-0.00}$	9.1
(14.1–45 keV)	$0.084^{+0.002}_{-0.000}$	$0.110^{+0.003}_{-0.007}$	0.18	$-0.986^{+0.034}_{-0.000}$	$1.9^{+1.1}_{-0.1}$	$-1.44^{+0.14}_{-0.00}$	16.2

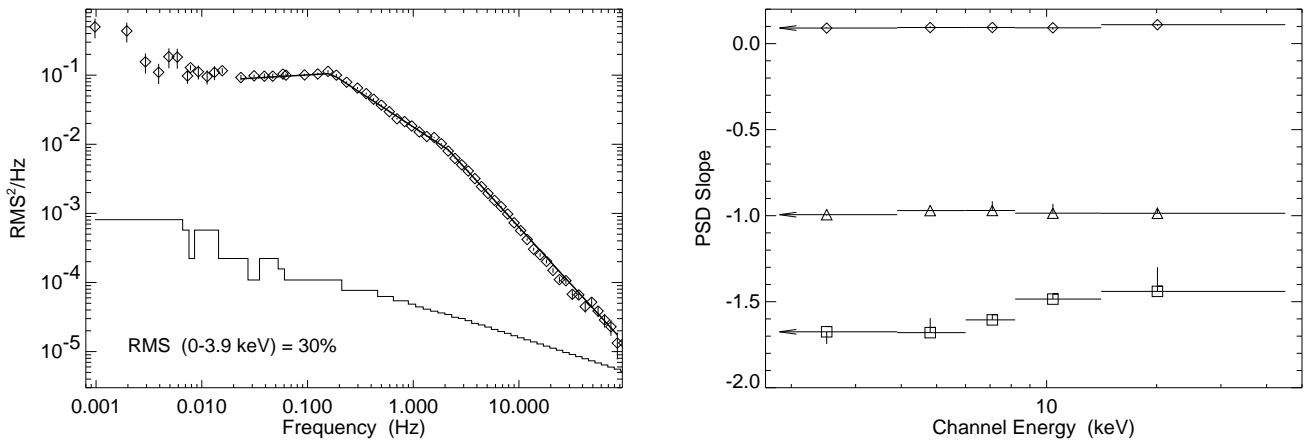


Fig. 2.— *Left*: The same (0–3.9 keV) PSD presented in Fig. 1, except that here we also show the best fit doubly broken power law (fit in the range 0.02–90 Hz, reduced $\chi^2 = 4.0$). *Right*: Best fit power law slopes, from doubly broken power law fits, as a function of channel energy. Diamonds are the slopes in the ≈ 0.02 –0.2 Hz range, triangles are the slopes in the ≈ 0.2 –2 Hz range, and squares are the slopes in the ≈ 2 –90 Hz range.

3. COHERENCE FUNCTION

3.1. The Coherence Function

Coherence is a lesser known and lesser used statistic than the power spectrum. Like the time delay, it is defined for two or more concurrent processes (cf. Bendat & Piersol 1986; Vaughan & Nowak 1997). It is closely related to the cross correlation function, and is particularly useful for studying processes whose power density spectra contain features, such as QPO or sudden changes in slope, because it provides a means of isolating for study a particular Fourier frequency or range of frequencies that are strongly correlated across energy bands.

The coherence function, $\gamma^2(f)$, is a Fourier-frequency-dependent measure of the degree of *linear* correlation between two concurrent time series. Specifically, it gives the fraction of the mean-squared variability at f of one time series that can be attributed to, or equivalently predicted from, the other.

Consider two statistically independent time series, $s(t)$ and $h(t)$, measured concurrently. In this work, we are interested in cases where s and h are X-ray light curves measured simultaneously in two energy channels. It is (almost) always possible to relate s and h by a linear transformation of the form

$$h(t) = \int_{-\infty}^{\infty} t_r(t-\tau)s(\tau)d\tau. \quad (5)$$

The function $t_r(\tau)$ is called the transfer function between s and h . In the frequency domain, eq. (5) becomes

$$H(f) = T_r(f)S(f) \quad (6)$$

where $S(f)$, $H(f)$, and $T_r(f)$ are the Fourier Transforms of $s(t)$, $h(t)$, and $t_r(t)$ respectively. Imagine making a sequence of measurements of $s(t)$ and $h(t)$, each of finite duration. If $T_r(f)$ is the same for each measurement of s and h , the processes are said to be perfectly coherent. That is, a measurement of one, say $s(t)$, enables us to predict the other, $h(t)$. The coherence function measures the degree to which $T_r(f)$ is constant for the data segments and Fourier frequencies over which we average. This is equivalent to a measure of the degree of linear correlation, in the fractional mean-squared sense, between s and h at f .

The coherence function is defined by

$$\gamma^2(f) = \frac{|\langle S^*(f)H(f) \rangle|^2}{\langle |S(f)|^2 \rangle \langle |H(f)|^2 \rangle}, \quad (7)$$

where triangular brackets denote an average over an ensemble of measurements. The one sigma uncertainty in $\gamma^2(f)$, in the case of Gaussian statistics, is

$$\delta\gamma^2(f) = \frac{\sqrt{2}\gamma^2(f)[1-\gamma^2(f)]}{|\gamma(f)|\sqrt{n}}, \quad (8)$$

where n is the number of measurements averaged in computing $\gamma^2(f)$ (Bendat & Piersol 1986; Vaughan & Nowak 1997).

The quantity within triangular brackets in the numerator, $S^*(f)H(f)$, is the cross power spectrum (sometimes called the complex cross spectrum or cross spectral density) between s and h . As discussed above, it is a complex quantity whose phase is a measure of the shift between the two light curves at f . The denominator in eq. (7) is the product of the average power spectra.

An intuitive feel for the coherence function may be gained by looking at it geometrically. Let the j th component of the

FFT of s (where we now consider an equispaced, discrete-time process s_k) be S_j , which we write as $S_j = |S_j|e^{i\phi_s}$. The product $S_j^*H_j$ is then equal to $|S_j||H_j|e^{i(\phi_h-\phi_s)}$. The coherence function is defined as the squared magnitude of the average value of this product, $|\langle S_j^*H_j \rangle|$, normalized by the product of the individual power spectral densities, $\langle |S_j|^2 \rangle \langle |H_j|^2 \rangle$.

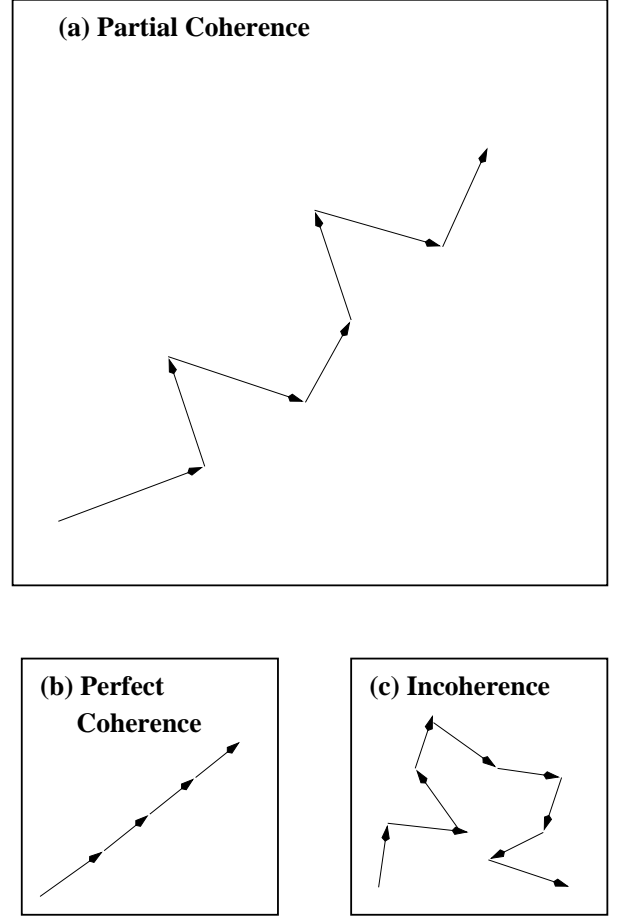


Fig. 3.— a) Vector illustration of the coherence function. Each vector is the complex number A^*B at a single Fourier frequency f for a single measurement of A and B . If the two processes are coherent, then A^*B will always have the same phase, as shown in (b). The vectors will be perfectly aligned and $|\sum A^*B|$ will be equal to $\sum |A^*B|$. If the processes are incoherent, then the phase of A^*B will be uniformly and randomly distributed on $[-\pi, \pi]$, as illustrated in (c). In this case, $\langle |A^*B|^2 \rangle / (\langle |A|^2 \rangle \langle |B|^2 \rangle) \rightarrow 0$ as the number of measurements approaches infinity.

The process of finding the average value $S_j^*H_j$ may be pictured as a vector sum in the complex plane. The sum may be found geometrically by drawing each term in the sum as a vector and adding them head to tail, as in usual vector addition, as shown in Figure 3a. If the time series are coherent at frequency f_j , then the phase difference between them, and hence the direction of the vector product $S_j^*H_j$, will be the same for each measurement in the sequence, as shown in Figure 3b. Geometrically, the vectors will all point in the same direction, and the sum of the vectors will have the same magnitude as the scalar

sum of their magnitudes. In this case, the numerator in eq. (7) will equal the denominator, and the coherence is unity. Coherence can only be computed over an ensemble of measurements.

In the opposite extreme, the soft and hard channels are completely incoherent. The phases of S_j and H_j are unrelated, and $\phi_h - \phi_s$ will be uniformly and randomly distributed on $[-\pi, \pi]$. This is just a 2-D random walk, as illustrated in Figure 3c. As the number of observations increases, the measured coherence goes to zero.

The light curves $s(t)$ and $h(t)$ need not look at all alike to be perfectly coherent. Indeed, they will look alike only if the time difference at each Fourier frequency, $\delta t = (\phi_h - \phi_s)/(2\pi f)$, is constant, which is equivalent to $t_r(\tau) = k\delta(\tau - \delta t)$, where k is a scaling factor between s and h .

An example of near perfect coherence can be found in the data studied for this paper. Figure 4 shows lightcurves of Cyg X-1 in the (0–3.9 keV) and (14.1–45 keV) energy bands. We have divided the data into 128 s segments for measuring coherence. The average direction in the complex plane of the Fourier transform of each segment over the Fourier frequency range 1.5–2.5 Hz is shown above the top light curve and below the bottom, labeled $\langle A \rangle$ and $\langle B \rangle$. The product $\langle A^* B \rangle$ is shown between the light curves. Notice that the phase of the Fourier transform varies randomly from segment to segment. In contrast, $\langle A^* B \rangle$ remains constant, indicating a fixed phase shift between the light curves in the 1.5–2.5 Hz range. As we will show later, the coherence is unity over a broad frequency range, even though the phase shift varies by a factor of 4 over the same range.

In practice, measurement noise (in our case Poisson counting noise) causes the measured coherence to be always smaller than unity. Poisson noise contributes a random part to each phase measurement, causing the $\langle S(f)^* H(f) \rangle$ to be slightly misaligned. For weak signals (relative to the noise), counting noise dominates the signal. Poisson noise always dominates at sufficiently high frequencies because it has a (nearly) white power density spectrum. Coherence is also difficult to measure at low frequencies because the number of independent measurement is smaller. Vaughan & Nowak (1997) discuss methods to correct γ^2 and $\delta\gamma^2$ for counting noise.

3.2. Coherence in Cyg X-1

In Figure 5 we present the coherence function for our Cyg X-1 observation. Specifically, the coherence function and its error bars were calculated by applying eq. (8) of Vaughan & Nowak (1997) to our data. (Strictly speaking that equation is most valid for the high coherence, high signal regime of our PSDs, which here is $f \lesssim 10$ Hz. Improved estimates using the more complicated formulae presented in Vaughan & Nowak (1997) are unlikely, however, to drastically change our results.) All comparisons shown are to the (0–3.9 keV) energy band. As discussed by Vaughan & Nowak (1997), the expectation from many theoretical models is that the coherence should be less than unity. As with previous observations of Cyg X-1 (Vaughan

1991; Vaughan & Nowak 1997; Cui et al. 1997b), the coherence is remarkably close to unity over a wide frequency range, even for rather disparate energy bands. Over the range 0.02–10 Hz, the coherence is nearly unity. In the two highest energy channels, there is a trend for the coherence to drop slightly above ≈ 1 Hz. In all energy channels, there is a trend for the coherence to drop below ≈ 0.02 Hz and above ≈ 10 Hz. For the most part, the deviation from unity coherence becomes greater with increasing energy. At the lower frequency end, the coherence recovers back towards unity near 0.005 Hz, coincident with the weak low frequency feature seen in the PSD.

Further of note is that in the 0.02–0.2 Hz range, energy band 5 is actually slightly more coherent than energy band 4 (both as compared to energy band 1). Due to the extremely good measurements in this frequency range, this difference is actually significant. The frequency regime 0.02–0.2 Hz corresponds to the flat part of the PSDs for energy bands 1–5.

We highlight these features in Figure 6 by presenting a grey scale plot of $\log[1 - \gamma^2(f)]$, which enhances the small differences from unity coherence. In this figure, high coherence is white, and low coherence is black. The lowest energy channel, by definition, is coherent with itself. The general trend to lose coherence at both low and high frequencies is evident in this plot, as is the trend for this loss to increase with energy. The highest energy channel does indeed appear more coherent in the 0.02–0.2 Hz range. Note that the high coherence coincident with the 0.005 Hz feature is also evident in Figure 6.

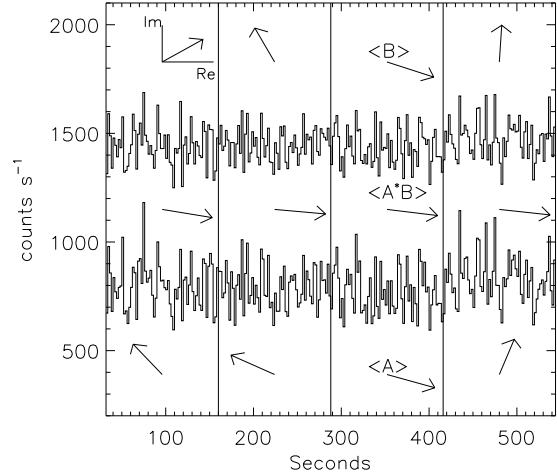


Fig. 4.— Lightcurves (solid lines) for a portion of our Cyg X-1 data. The top curve is the (14.1–45 keV) energy band, shifted by 600 cts s^{-1} , while the bottom is for the (0–3.9 keV) energy band. Solid vertical lines divide the data into segments of 128 s. Arrows represent the *directions* in the complex plane of the FFT and cross power spectral density for each data segment, averaged over the frequency range 1.5–2.5 Hz. Poisson noise has *not* been subtracted; therefore, it is expected that $\langle A^* \rangle \langle B \rangle \neq \langle A^* B \rangle$, as seen for these data.

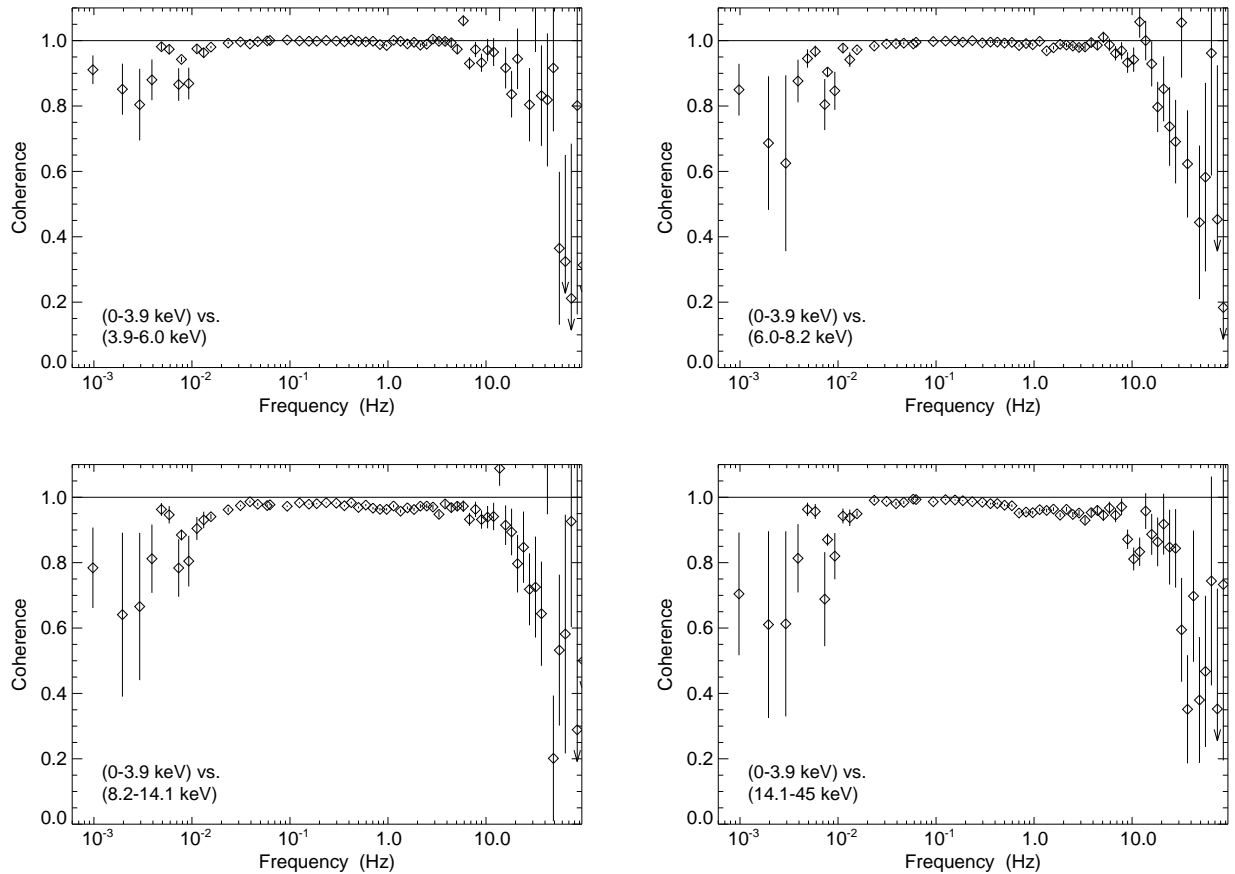


Fig. 5.— Coherence, as a function of Fourier frequency, for various energy bands vs. the lowest energy band (0–3.9 keV). (Solid line is coherence equals unity.) Error bars are calculated from eq. (8).

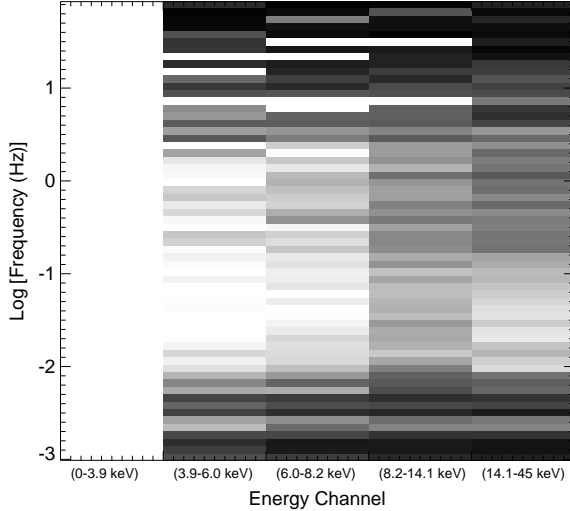


Fig. 6.— Grey scale representation of the coherence function as a function of frequency (vertical axis) and energy band (horizontal axis). Specifically, there are 256 grey scale levels corresponding to the value of $\log[1 - \gamma^2(f)]$, where $\gamma^2(f)$ is the noise-subtracted coherence function for the indicated energy band as compared to the (0–3.9 keV) energy band. Values of $\gamma^2(f) > 0.999$ were set to 0.999. White corresponds to the highest coherence levels, black to the lowest coherence levels.

The deviations to greater than unity for the noise-subtracted coherence in Figures 5 and 6 are due to both statistical *and* systematic errors. As the coherence function is a fourth order statistic [as compared to a second order statistic like the PSD, cf. Bendat & Piersol (1986)], it is very sensitive to uncertainties in the noise subtraction. With a systematic uncertainty in the deadtime as large $\lesssim 25\%$, and even with the background variability levels as seen in Figure 1, we are still *very* confident of the coherence estimates from $\approx 10^{-3}$ –30 Hz, where systematic uncertainties are essentially negligible. Between ≈ 30 –100 Hz, our estimates are that systematic uncertainties increase the shown error bars by no more than $\approx 30\%$. The noise-subtracted coherence points do show that our noise subtraction is not perfect; however, the general trend of coherence loss is likely fairly secure to ≈ 100 Hz.

4. TIME LAGS

4.1. Simple Considerations

The Fourier time delay, or lag, is also computed for two concurrent and correlated time series. Like the coherence, it is related to the cross correlation, and is a Fourier-frequency dependent measure of the time delay between the time series (cf. Miyamoto & Kitamoto 1989; Miyamoto et al. 1992; van der Klis 1989).

As in §3, let $s(t)$ be a discretely and uniformly sampled “soft energy” lightcurve and $h(t)$ be a discretely and uniformly sampled “hard energy” lightcurve. These lightcurves, as for the PSD (cf. §2) and coherence (§3), are divided into data segments of uniform length and an FFT is performed on each segment. The Fourier phase lag, $\phi(f)$, is the phase of the *average* cross power spectrum. That is, $\phi(f) = \arg[C(f)]$, where

$$C(f) = \langle S^*(f)H(f) \rangle. \quad (9)$$

The Fourier time lag is constructed from $\phi(f)$ by dividing through by $2\pi f$, i.e. $\tau(f) \equiv \phi(f)/2\pi f$. The Fourier time lag

can be either positive or negative. For our sign convention, a positive time lag indicates that the hard light curve lags the soft light curve. Note that the Fourier phase is defined on the interval $(-\pi, \pi)$, hence a lag of $\pi/2$ in reality could be a lead of $3\pi/2$. For a further discussion, see Nowak & Vaughan (1996).

In general, both the phase lag and time lag are non-constant functions of Fourier frequency, f . To get a feel for what this can mean, consider the following simple example. Imagine we have a source of fluctuations that produces soft X-ray photons some distance from a region that also responds to these fluctuations by producing hard X-ray photons. If the fluctuations can propagate from the soft-photon-producing region to the hard-photon-producing region, without dispersion, then we expect a time delay between the soft and hard photons that is *independent of Fourier frequency*, f . The time delay at all Fourier frequencies will simply be the distance between the soft X-ray source and the hard X-ray response divided by the propagation speed. This means that the Fourier phase lag, $\phi(f)$, will increase linearly with f (modulo integer multiples of 2π).

If the two processes are perfectly correlated (cf. §3), the two processes are related by a constant, linear transfer function. The time lags observed in Cyg X-1 are not independent of Fourier frequency; however, the phase lags are roughly independent of f . Let us look at a crude but illustrative transfer function that produces a constant phase lag. Specifically, we consider a transfer function, $T_r(f)$, with both constant phase and amplitude. This simple example is in fact a reasonable approximation to Cygnus X-1. In this case, we can write

$$H(f) = A \exp(\pm i\Delta\phi) S(f), \quad (10)$$

where both A and $\Delta\phi$ are real constants. The plus sign is for $f > 0$ and the minus sign is for $f < 0$, because the Fourier transform of a real time series satisfies $H(f) = H^*(-f)$. Taking the inverse transform of $A \exp(\pm i\Delta\phi)$, the transfer function, $t_r(\tau)$, can be written in the time domain as

$$t_r(\tau) = A \left[\cos(\Delta\phi)\delta(\tau) + \frac{\sin(\Delta\phi)}{\tau} \right]. \quad (11)$$

That is, a fraction $A \cos(\Delta\phi)$ of the hard variability is exactly coincident with the soft variability, while a (typically smaller) fraction is delayed from the soft variability with a τ^{-1} “tail” in the transfer function. For $A \sim 1$ and $\Delta\phi \sim 0.1$ radians, most of the soft and hard lightcurves are exactly coincident with one another, and only a small fraction of the hard photons lag behind the soft. To illustrate the above points, we present examples of both constant (as a function of Fourier frequency) time lags and constant phase lags in Figure 7.

The time delays between hard and soft photons may be due to a physical separation between a source and a response, as in the first example, or they may be related to the emission process itself. For the case of Comptonization, hard photons undergo more scatterings than soft photons and therefore are naturally delayed from soft photons. This latter process occurs on very short timescales (on the order of the light crossing time of the Comptonizing region) and represents the *minimum* expected time delay between hard and soft X-rays within the context of this particular model (Miyamoto & Kitamoto 1989; Miller 1995; Nowak & Vaughan 1996; Kazanas, Hua & Titarchuk 1997). On the other hand, the *maximum* expected time delay between hard and soft X-rays will be less than the size of the

emitting region divided by the *slowest* propagation speed in that region (whether it be a sound speed or a thermal wave speed, etc.). As discussed below, most of the hard and soft photons seen in Cyg X-1 are nearly temporally coincident, and therefore the (possibly extended) sources of soft and hard X-rays are likely to be nearly spatially coincident as well. The more spatially coincident the soft and hard X-ray sources/responses are, the shorter the observed time delays will be.

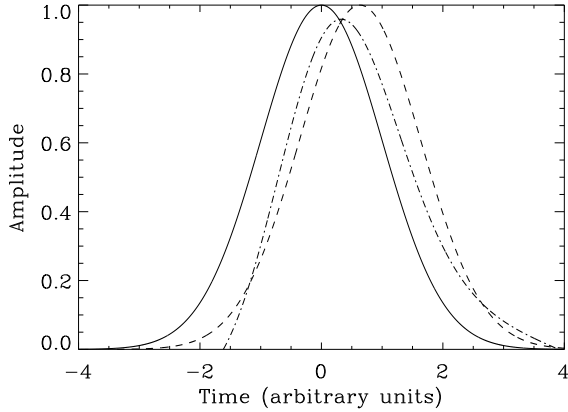


Fig. 7.— Gaussian of unit amplitude and variance (solid curve), and same Gaussian shifted in time by $\Delta t = 0.5$ units (dashed line) and in phase by $\Delta\phi = 2\pi f_0 \Delta t$, (dot-dashed line) where f_0 is the lowest Fourier frequency (here $f_0 = 1/8$). Notice that both cause a shift to later times, while the constant phase shift also induces an extended tail.

4.2. Noise Limits on Time Lag Measurements

A geometrical interpretation of the phase/time lags is helpful in elucidating their nature (cf. §3.1). To understand the effects of counting noise on measurements of the time lags, we again consider the Fourier components of a measured process as vectors in the complex plane. The vectors consist of the sum of a signal part and a noise part. Let the measured Fourier components in the soft and hard channels be given by $S(f) \equiv A_s(f)f^{-\alpha_s} + A_s^{(N)}(f)$ and $H(f) \equiv A_h(f)f^{-\alpha_h} + A_h^{(N)}(f)$. Here A_s and A_h are complex quantities representing the signal that have a constant amplitude, but have phases (i.e. directions in the complex plane) that are a function of frequency, f . The quantities $A_s^{(N)}$ and $A_h^{(N)}$ are the noise components of the Fourier transforms. They have a well defined mean amplitude but a completely random phase. The phases of the noise components—and thus their orientation in the complex plane—vary randomly from frequency to frequency and from data segment to data segment. For simplicity, we shall take $A_s(f)f^{-\alpha_s} = A_h(f)f^{-\alpha_h} = A(f)f^{-\alpha}$ and $|A_s^{(N)}(f)| = |A_h^{(N)}(f)| = \sqrt{P_N}$, which is approximately true for our Cyg X-1 data.

As for the coherence function, when we average the CPD over discrete samples of the lightcurve and/or over frequency bins, we are essentially summing vectors in the complex plane. For unity coherence, the signal vectors each have constant directions set by the phase lags and amplitudes set by the PSD (here equal to $A^2 f^{-2\alpha}$). More generally, if we sum the signal over N lightcurve samples and/or frequency bins, the total

length of the summed signal vectors becomes

$$N \sqrt{\gamma^2(f)} |A|^2 f^{-2\alpha}, \quad (12)$$

where the factor of $\sqrt{\gamma^2(f)}$ takes account of the coherence function (see §3). In our data set, however, the coherence function is unity below ~ 10 Hz, and falls off rapidly at higher frequencies.

The noise vectors associated with the cross power spectral density each have a mean amplitude of $2\sqrt{P_N}|A|f^{-\alpha}$ (i.e. twice the product of the amplitude of an individual noise vector with the amplitude of an individual signal vector). Their phases, however, are completely random. Thus, in the averaging process the sum of these noise vectors looks like a random walk in the complex plane (Vaughan 1991, and §3.1 above). The root mean square amplitude of the sum of the noise vectors is therefore

$$\sqrt{2N P_N} |A| f^{-\alpha}. \quad (13)$$

The fact that this sum has a random phase leads to the uncertainty in the phase lag determination. In the small angle approximation (appropriate for large N), the uncertainty of the phase lag is then of order the expectation value of the magnitude of the sum of the noise vectors divided by the mean magnitude of the sum of the signal vectors. We have:

$$\Delta\phi(f) \approx \sqrt{\frac{P_N}{N \gamma^2(f)}} \frac{f^\alpha}{|A|}. \quad (14)$$

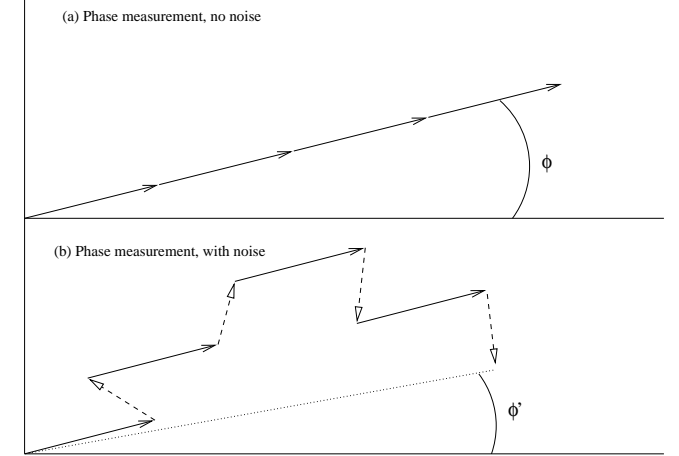


Fig. 8.— The process of measuring a phase lag in the presence and absence of noise, illustrated as a vector sum in the complex plane for the case of perfect coherence. Signal vectors are displayed as solid lines in (a) and (b), and noise vectors as dashed lines in (b). For perfect coherence, all signal vectors are aligned, as seen in (a) and (b). The noise vectors in (b) have phases uniformly and randomly distributed on $[-\pi, \pi]$, and contribute component to the vector sum with random phase and an amplitude that grows as the square root of the number of measurements. In contrast, the amplitude of the sum of signal vectors grows as the number of measurements.

The process of measuring a phase lag in the presence and absence of noise is illustrated in Figure 8 for the case of perfect coherence. All signal vectors, displayed with solid lines, are aligned. The noise vectors, displayed as dashed lines, have phases uniformly and randomly distributed on $[-\pi, \pi]$. The

noise vectors contribute a random component to the vector sum. The noise component has random phase, and an amplitude that grows as the square root of the number of measurements. In contrast, the amplitude of sum of signal vectors grows as the number of measurements.

Typically, one has total observing time T segmented into lightcurves of length T_s (yielding a minimum Fourier frequency $1/T_s$). The FFTs are also logarithmically binned over a frequency interval with *fractional* width d . The total number of Fourier components averaged at frequency f is then just the total number of lightcurves, T/T_s , times the number of frequency bins averaged, df/T_s^{-1} , yielding $N = dTf$. For the PSD normalization used in §2, $|P_N| \approx 2/\mathcal{R}$, independent of frequency. We then have

$$\Delta\phi(f) \approx 2 [dT\mathcal{R}\gamma^2(f)]^{-1/2} |A|^{-1} f^{\alpha-1/2}. \quad (15)$$

For our Cyg X-1 data $\gamma^2(f) \approx 1$ and $\alpha \sim 0.5$ (i.e. PSD $\propto f^{-1}$) in the frequency range ~ 0.2 – 2 Hz; therefore, $\Delta\phi(f)$ is approximately constant. Above ~ 2 Hz, $\alpha \sim 0.7$ – 0.9 and $\gamma^2(f)$ begins to drop rapidly. It therefore becomes difficult to measure phase/time lags above ~ 30 Hz. This situation is not easily improved, even with *substantially* longer integration times.

As discussed below, the phase lags in Cyg X-1 are roughly $\propto f^{0.3}$ (i.e. time lags $\propto f^{-0.7}$), and $\Delta\phi$ is comparable to the noise near 0.1 Hz. As $\alpha \sim 0.5$, the weak, positive dependence of phase lag on frequency is what allows us to detect the phase/time lags in the 0.1–30 Hz range. Below $f \sim 0.1$ Hz, $\alpha \sim 0$, and therefore $\Delta\phi/\phi \propto f^{-0.8}$, assuming $\phi \propto f^{0.3}$. The phase/time lags therefore become undetectable below ~ 0.1 Hz. Extending our measurements to a decade lower in Fourier frequency would require an integration time of order 40 times longer. In Figure 9, we present these idealized estimates of the noise limit for parameters characteristic of our observations.

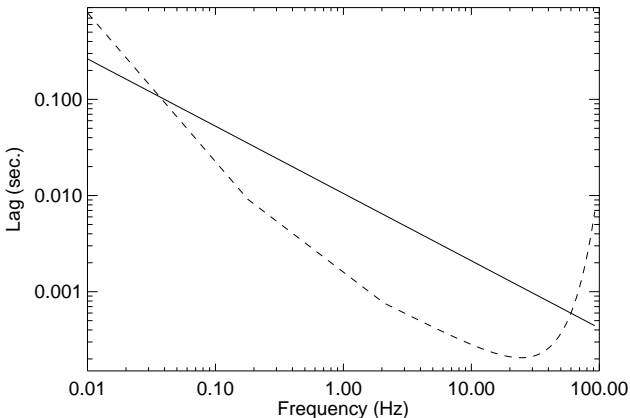


Fig. 9.— The dashed line is the idealized estimate of the noise level for time lag measurements typical in this paper [cf. eq. (15)]. We have used the double broken power law fit and count rate for the (0–3.9 keV) energy band in our estimate, and we have taken $\gamma^2(f) = \exp[-(f/30 \text{ Hz})^2]$. The solid line is an idealized representation of the time lag we see between our lowest and highest energy bands. For frequencies below ~ 0.1 Hz and above ~ 30 Hz, lags cannot be measured because of noise limitations.

As discussed by Bendat & Piersol (1986), we can make these noise estimates more rigorous. Specifically, the estimate that we use for the uncertainty in the phase is

$$\Delta\phi(f) = N^{-1/2} \sqrt{\frac{1-g(f)}{2g(f)}}, \quad (16)$$

where N , as before, is the number of lightcurves and/or frequency bins averaged over and $g(f)$ is defined as

$$g(f) \equiv \frac{|\langle S^*(f)H(f) \rangle|^2}{\langle |S(f)|^2 \rangle \langle |H(f)|^2 \rangle}. \quad (17)$$

In the above, $S(f)$ and $H(f)$ are the Fourier transforms of the two light curves to be compared *without* Poisson noise subtracted. This formula has the properties discussed above (including taking account of the coherence function, cf. §3), and provides a more rigorous estimate of the errors in the phase lag than simple error propagation estimates (e.g., Cui et al. 1997b). In fact, $g(f)$ is simply the *measured* coherence of the two light curves, *without* correcting for counting noise. The error in the time lag is then simply given by $\Delta\tau(f) = \Delta\phi(f)/2\pi f$.

4.3. Time Lags in Cyg X-1

In Figure 10, we present the time lags vs. Fourier frequency for energy bands 2–5 vs. energy band 1. The measurements are above the noise level, as defined by eq. (16), from 0.1–30 Hz. Within this frequency range, the data are consistent with the softest energy band *always* leading the harder energy bands. Those frequency points where the hard leads the soft are dominated by Poisson noise fluctuations.

Some general properties of the observations are notable. First, the time lags between all channels approximately show a power law dependence upon Fourier frequency, $\tau(f) \propto f^{-0.7}$, although there are significant deviations from a simple power law. This is consistent with previous observations of the low state of Cyg X-1 (Miyamoto & Kitamoto 1989; Miyamoto et al. 1992; Crary et al. 1998). As discussed in §4.1, such a frequency dependence is closer to a constant phase lag (as a function of Fourier frequency) than a constant time lag. The time lags presented in Fig. 10 correspond to Fourier phases ranging from 0.01 (low Fourier frequency, energy band 2 vs. energy band 1) to 0.2 radians (high Fourier frequency, energy band 5 vs. energy band 1). In terms of a constant phase lag transfer function interpretation [cf. eq. (11)], this means that nearly all of the hard and soft flux variations occur quasi-simultaneously, with only a small fraction of the hard photons lagging the soft photons.

The $f^{-0.7}$ dependence of the time lag also implies a large dynamic range in delay times, on the order of a decade and a half. The longest time lags are 0.05 sec. Measured as a light crossing time, this corresponds to a distance of $10^3 GM/c^2$, for $M = 10 M_\odot$. Between energy band 5 and energy band 1, the shortest measured time lag is $\approx 10^{-3}$ sec, which corresponds to a light crossing radius of $20 GM/c^2$ for $M = 10 M_\odot$. It is this large dynamic range in characteristic length scales associated with the variability, as further discussed in §5, that is difficult for theoretical models to address (although see Kazanas, Hua & Titarchuk 1997). However, if one were to invoke slower “propagation speeds” (see also paper III), the implied length scales would be commensurately shorter. If one were to restrict the size scale to $50 GM/c^2$, the longest time lags would imply propagation speeds of $0.05 c$. As discussed in paper III, this is uncomfortably slow for both Advection Dominated Accretion Flow (ADAF) models, where one expects the matter in the inner regions to be nearly in radial free fall (cf. Narayan 1996), and Compton corona models, where the sound speed of the corona is a sizable fraction of c .

The time lags generally increase with energy band separation. We quantify this statement in §5 below. This increase can be reconciled with either the notion that “propagation path” from soft source to hard response increases with energy separation, or that the “propagation speed” from soft source to hard response decreases with energy separation. We also note that the time lags between bands 1 and 5 are consistent with the sum of the time lags from bands 1 to 2, bands 2 to 3, bands 3 to 4, and bands 4 to 5.

5. PHYSICAL INTERPRETATIONS

5.1. PSD Shape

In paper III, we consider in detail the implications of our timing analysis to the specific Comptonization model that we presented in paper I. We also consider in more general terms the implications of our timing analysis for ADAF models. Specifically, we investigate the phenomenology of what we dub “propagation models”, and derive constraints on likely propagation speeds for disturbances in a disk. Here, however, we adopt a slightly more general approach.

We still wish to consider the implications of Comptonization models; however, rather than discuss a specific model, we will consider those effects that we generally expect to find. As we have discussed elsewhere (Nowak & Vaughan 1996, and refer-

ences therein), if the source of the observed variability is from soft photons, perhaps from an accretion disk, that are subsequently upscattered by a Comptonizing medium, then we expect a number of effects to be evident.

First, at high Fourier frequencies, we expect that dispersion in the scattering times in the Comptonizing medium will lead to an attenuation in the variability amplitude. This attenuation will be manifested as a (typically exponential) rollover in the PSD on timescales shorter than the typical diffusion timescale through the Comptonizing medium (Brainerd & Lamb 1987; Kylafis & Klimis 1987; Wijers, van Paradijs & Lewin 1987; Stollman et al. 1987; Bussard et al. 1988; Kylafis & Phinney 1989; Miller & Lamb 1992; Miller 1995; Nowak & Vaughan 1996). As discussed in Nowak & Vaughan (1996), the *simplest* expectation is an exponential rollover in the PSD that is $\propto \exp[-(f\tau)^2]$, where $\tau \approx 2\pi\sqrt{N\bar{\lambda}_{\text{es}}}/c$. Here, N is the number of scatters that the photon has undergone, and $\bar{\lambda}_{\text{es}}$ is the mean free path between scatters. If the optical depth of the Comptonizing medium is ≈ 1 , then $\bar{\lambda}_{\text{es}} \approx R$, where R is the size of the medium.

In the simplest models of Comptonization (cf. Pozdnyakov, Sobol & Sunyaev 1983, and references therein), one expects the number of scatters N to be of the order

$$N \sim \frac{mc^2}{4kT} \ln \left(\frac{E_o}{E_s} \right) , \quad (18)$$

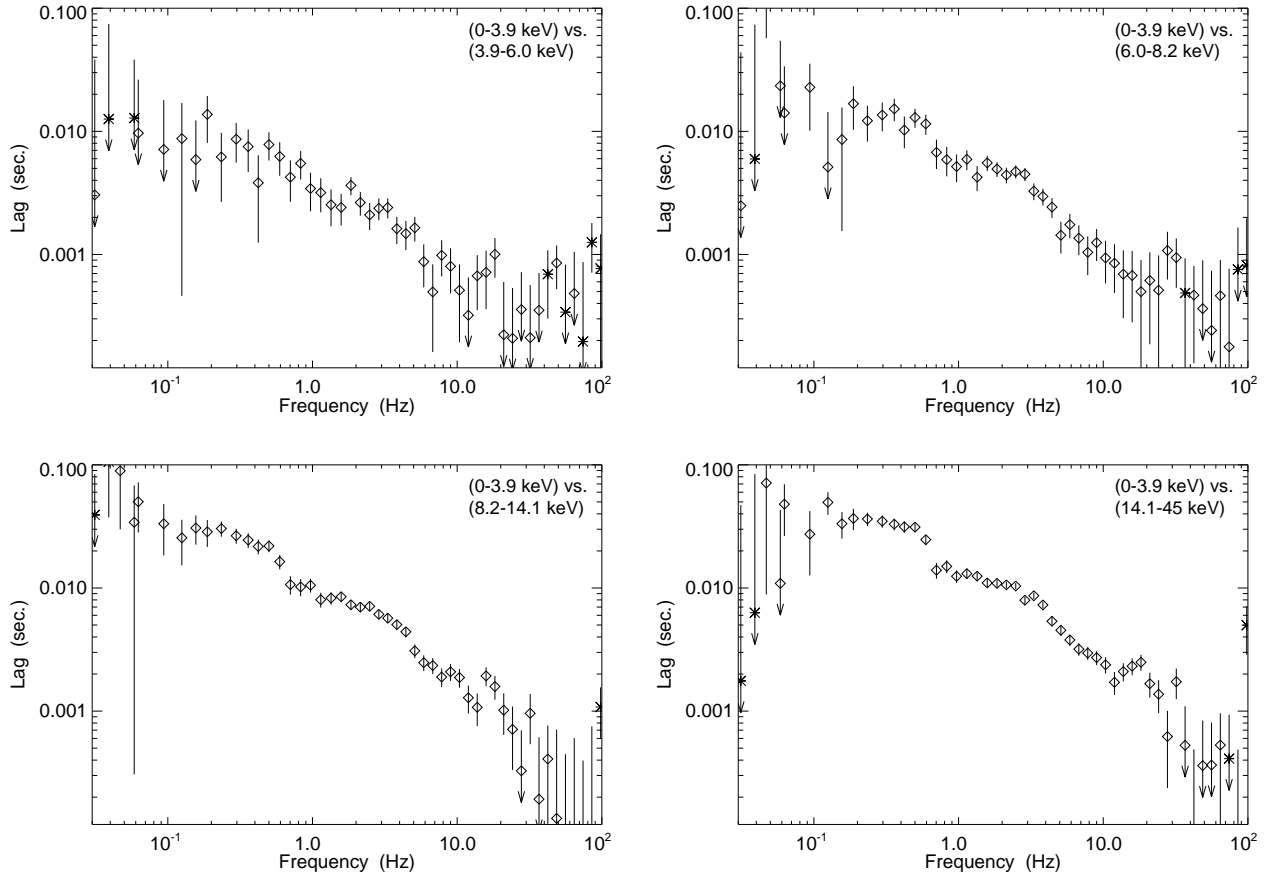


Fig. 10.— Time lags, as a function of Fourier frequency, for various energy bands vs. the lowest energy band (0–3.9 keV). Diamonds represent hard lagging the soft, whereas asterisks represent soft lagging the hard. Error bars are calculated from eq. 16. Measurements are above the noise level in roughly the range of 0.1–30 Hz.

where T is the temperature of the Comptonizing medium, E_s is the energy of the soft input photons, and E_o is the energy of the observed output photons. For a very simple Compton cloud model, one therefore expects an exponential cutoff frequency, $f_c \equiv \tau^{-1}$, on the order of

$$f_c \approx 50 \text{ Hz} \frac{(R/50 \text{ GM}/c^2)^{-1} (kT/80 \text{ keV})^{1/2}}{[\ln(E_o/1 \text{ keV}) - \ln(E_s/0.2 \text{ keV}) + 1.6]^{1/2}}, \quad (19)$$

where we have taken $M = 10 M_\odot$ and where we have chosen a characteristic coronal radius and temperature consistent with the spectral model of paper I.

In Figure 11 we show the results of fitting an exponentially cutoff power law to the PSDs of §2. For all the energy bands, we fit functions of the form $af^b \exp[-(f/f_c)^2]$ to the 3–90 Hz data. The reduced χ^2 for the fits ranged from 1.8 for the lowest energy band to 5.2 for the highest energy band. Again, reduced χ^2 as large as these are partly indicative of the extremely small error bars associated with the data, as well as the fact that a cutoff powerlaw is only a qualitative description of the data. As also discussed in §2 and shown in Figure 11b, the PSD slope “hardens” as one goes to higher energy bands. The best fit slopes ranged from -1.74 for the lowest energy band to -1.4 for the highest energy band. The change in slope is significant and appears to be proportional to the log of the band energy.

Although exponential cutoffs are allowed for all the energy bands, fitting pure power laws (as was done in §2) results in nearly equally good fits. Based upon eq. (19), we would have expected much stronger cutoffs, if the source of the high frequency variability is intrinsic to the soft input photons⁴. We have fit a function of the form of eq. (19) to our best fit cutoff frequencies, which we present in Figure 11c. The best fit numerator was 123 Hz [i.e. $(R/50 \text{ GM}/c^2)^{-1}(kT/80 \text{ keV})^{1/2} \approx 2.5$], and the best fit soft input energy was $E_s = 2 \text{ keV}$. We emphasize that we do not consider this a detection of an exponential rollover, but more of an upper limit to the degree of rollover (or equivalently a lower limit to the cutoff frequency, f_c). In Figure 11c we present the cutoff frequencies that we naively would have expected if $E_s = 0.2 \text{ keV}$ (dashed line); however, we have kept the numerator as 123 Hz. The expected value of the exponential cutoff frequencies are somewhat lower than the values permitted by the data. (We further discuss this point in paper III.)

The simplest explanation (although see Kazanas, Hua & Titarchuk 1997 and §5.3 below) for the increase in the PSD “hardness” with energy and for the lack of a strong rollover in the high energy PSD is that the high frequencies do not represent variability intrinsic to the soft input source, but rather are the result of *direct* modulation by fluctuations in the Comptonizing medium itself. As we expect the Comptonizing medium to be both very hot and concentrated near the compact object where the dynamical timescales are the shortest (cf. paper I), it is natural to expect the corona to show harder PSD slopes at higher energies.

We hypothesize that the PSD above the break at $\approx 2 \text{ Hz}$ is dominated by fluctuations of the corona on dynamical timescales. As discussed in Vaughan & Nowak (1997) and in §5.4 below, this is also qualitatively consistent with the loss of coherence seen at these high frequencies. We further consider the characteristic PSD frequencies below.

⁴Note that this statement is true for a relatively spatially compact source. In the model of Kazanas, Hua & Titarchuk (1997), the *entire* PSD is reprocessed white noise from a soft input source. The range of power law slopes is achieved by distributing the Compton scatterings over several decades in radius of the system. We elaborate upon this point further in §5.3.

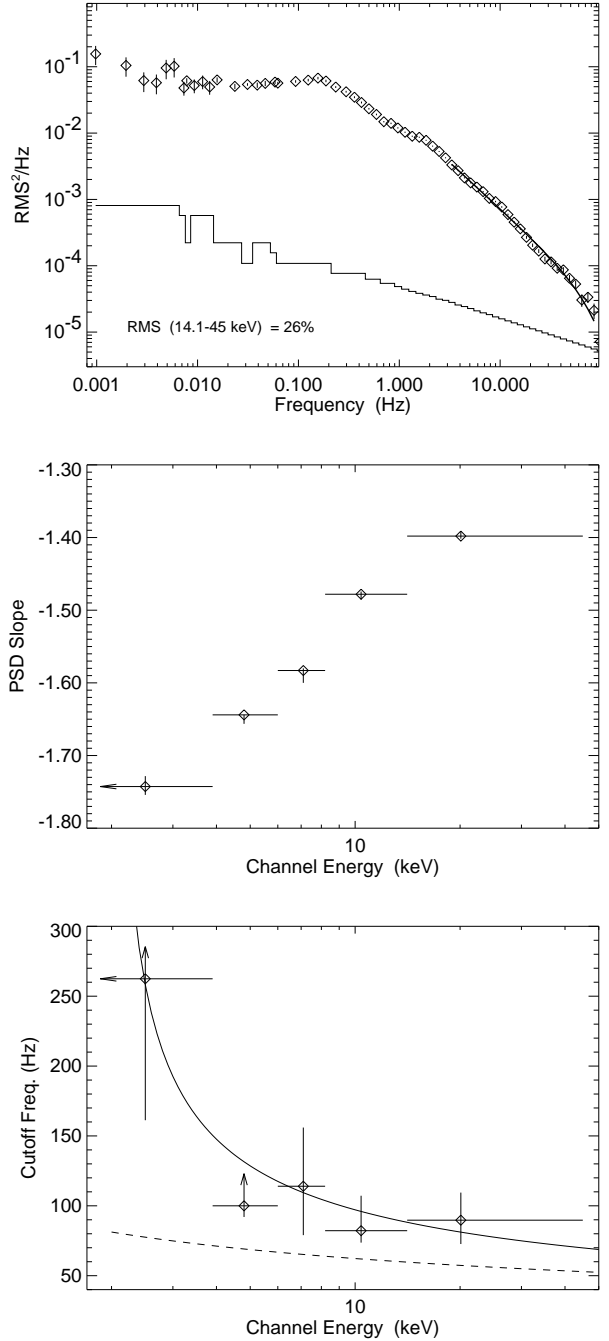


Fig. 11.— *Top*: The same energy band 5 PSD as presented in Fig. 1 with an exponentially cutoff power law fit to the 3–90 Hz data. *Middle*: Best fit power slopes to the 3–90 Hz PSD data as a function of channel energy. *Bottom*: Best fit cutoff frequency (solid line), using eq. (19). The best fit numerator is 123 Hz with $E_s = 2 \text{ keV}$. For the dashed line we have fixed the numerator of eq. (19) to 123 Hz, but have taken $E_s = 0.2 \text{ keV}$.

5.2. Characteristic Timescales of the PSD

The Compton corona model that we presented in paper I consisted of a spherical, central hot cloud surrounded by a thin, cold disk. The temperature at the inner edge of the cold disk was taken to be 200 eV, and there was evidence for an iron line with equivalent width ≈ 40 eV (cf. §1.3). These latter two facts, considering that the model was reasonably consistent with the data, suggest a radius for the Compton corona of approximately $50 GM/c^2$ if $M = 10 M_\odot$. Substantially smaller radii would imply a hotter temperature on the inner edge of the disk, which is not consistent with the data (Dove et al. 1998). Substantially larger radii would imply very weak iron lines, unless a substantial fraction of the coronal energy release were also at large radii, as in the model of Kazanas, Hua & Titarchuk (1997).

Taking $50 GM/c^2$ as a characteristic radius, we have the following characteristic timescales for a $10 M_\odot$ black hole accreting at approximately 5% L_{Edd} (cf. Table 1). The light crossing timescale is of order 2.5×10^{-3} sec, which is of order the shortest Fourier time lags seen in the system. The dynamical timescale (i.e., the Keplerian orbital period) is 0.1 s, or an orbital frequency of 9 Hz. This is of the same order as the location of the break in the PSD at ≈ 2 Hz, and is also consistent with the Fourier frequencies above which the soft and hard X-ray become incoherent with each other. This further supports our hypothesis that the variability above ≈ 2 Hz is dominated by *direct* modulation of the corona at radii $\lesssim 50 GM/c^2$. We again note that there is no evidence for any energy dependence of the PSD slopes below 2 Hz.

The characteristic viscous timescale is of order the dynamical timescale divided by the Shakura-Sunyaev α -parameter and by the square of the fractional Eddington luminosity (Shakura & Sunyaev 1973; Shakura & Sunyaev 1976). Thus this timescale is of $\mathcal{O}(50-500)$ s, or equivalently $\mathcal{O}(2 \times 10^{-3}-2 \times 10^{-2}$ Hz), for $\alpha \sim 0.1-1$. Characteristic thermal timescales are of the order of the dynamical timescale times the α -parameter, i.e. 1 s for $\alpha \approx 0.1$. The break in the PSDs at ≈ 0.2 Hz could therefore be associated with a characteristic viscous timescale or thermal timescale. The PSD $\propto f^{-1}$ between 0.2–2 Hz could be indicative of viscous and/or thermal fluctuations over a range of radii $\lesssim 50 GM/c^2$. Alternatively, one might wish to associate this portion of the PSD with dynamical timescale fluctuations at radii $\gtrsim 50 GM/c^2$.

The feature at $\approx 5 \times 10^{-3}$ Hz is somewhat problematic. This frequency is at the lower end of what we would associate with a characteristic viscous timescale (unless α is even smaller than 0.1), and is too slow for either a thermal or dynamical timescale unless it is associated with a very large radius ($R \approx 3 \times 10^4 GM/c^2$ for a dynamical timescale). We again stress, however, that based upon the PSDs alone, the evidence for a low frequency QPO is very weak.

5.3. Implications of the Time Lags

The time lags seen in Cyg X-1 are often interpreted in terms of Comptonization models (cf. Cui et al. 1997b; Kazanas, Hua & Titarchuk 1997; Crary et al. 1998 and references therein). Taking the simplest Comptonization models, one naturally expects the hard photons to lag behind the soft photons as the hard photons have undergone more scatters. The expected time delay is therefore proportional the difference in the average number of scatters required to reach the hard energy channel compared to the soft energy channel times the average distance traveled between scatters. Again taking the electron scattering op-

tical depth ≈ 1 so that $R \approx \bar{\lambda}_{\text{es}}$, the expected time delay is of the order

$$\Delta\tau \approx 1.6 \left(\frac{R}{50 GM/c^2} \right) \left(\frac{kT}{80 \text{ keV}} \right) \ln \left(\frac{E_H}{E_S} \right) \text{ ms} , \quad (20)$$

where E_H is the energy of the hard energy channel and E_S is the energy of the soft energy channel. (As before, we have taken $M = 10 M_\odot$.)

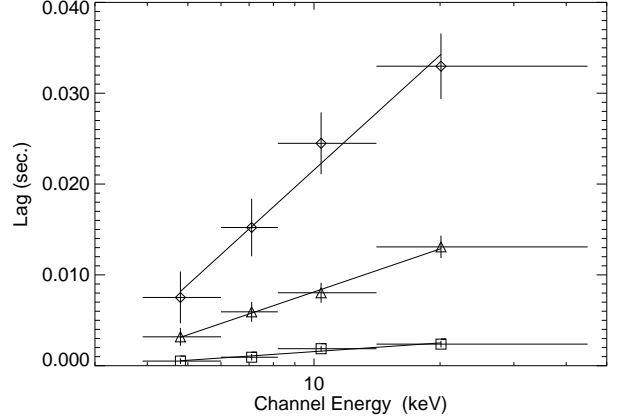


Fig. 12.— Time lags as a function of energy compared to the lowest energy band, (0–3.9) keV, for three different Fourier frequencies. Diamonds are for 0.3 Hz, triangles are for 1 Hz, and squares are for 10 Hz. Lines are the best fit functions of the form of eq. (20).

In Figure 12 we present the time delay, compared to the lowest energy band, as a function of energy for three frequencies, 0.3 Hz, 1 Hz, and 10 Hz. As has been noted recently for other observations (Cui et al. 1997b), the time delays do indeed increase nearly linearly with the log of the band energy. We have fit a function of the form of eq. (20) to these data, and find the best fit intercept to be given for $E_S \approx 3.0-3.2$ keV, in reasonable agreement with the average energy of 2.5 keV for the lowest energy channel. (We *did not* include a 0 sec time delay between the lowest energy band and itself in the fits, and the y-intercept was a free parameter.) Other authors (e.g. Cui et al. 1997b; Crary et al. 1998) recently have claimed that this previously observed logarithmic energy dependence of the time lag is strong evidence for the presence of a Compton corona; however, rarely do they note the fact that although the functional form agrees, the best fit slopes are apparently functions of Fourier frequency.

Specifically, if we set $kT = 80$ keV in eq. (20), then we find best fit values of $R = 230 GM/c^2$ for $f = 0.3$ Hz, $R = 85 GM/c^2$ for $f = 1$ Hz, and $R = 17 GM/c^2$ for $f = 10$ Hz. Any individual Fourier frequency agrees well with the simple expectations of Comptonization theory; however, taken as a whole the time delays *do not* agree with the *simplest* Comptonization models. This fact was originally noted by Miyamoto & Kitamoto (1989). Two possibilities have been suggested for maintaining the logarithmic energy dependence, yet creating the large dynamical range in time delays, within the context of Comptonization. The first is the possibility that the time delays are inherent to the source of soft input photons and are merely “re-processed” by the Comptonizing medium (Miller 1995; Nowak & Vaughan 1996). We explore this possibility in detail in paper III.

The second suggestion is that the dynamic range in time delays reflects a large range in radii of a Comptonizing medium (Kazanas, Hua & Titarchuk 1997). Specifically, Kazanas, Hua & Titarchuk (1997) posit a uniform temperature corona with essentially equal optical depth per decade of radius (i.e., electron density approximately $\propto r^{-1}$) that extends for roughly three decades in radius. A white noise (i.e., flat PSD) input spectrum is reprocessed into a power law PSD that shows time delays comparable to those shown in Figure 12. Specifically, the time delays, at a given Fourier frequency, show a logarithmic energy dependence, and higher Fourier frequencies show shorter time delays. This latter attribute is due to the fact that any portion of the lightcurve that comes from photons that have scattered over large distances has its high frequency variability strongly attenuated [cf. eq. (19)]. Any observed high frequency variability is *only* sampling those photons that have scattered over short distances, and therefore it will show relatively short time delays between soft and hard photons. Furthermore, the r^{-1} density profile means that there is roughly equal probability of scattering on length scales in any given decade of radius, which leads to the observed dynamic range in the time delays. Although the model of Kazanas, Hua & Titarchuk (1997) is consistent with the data, it is difficult to understand how such a configuration would evolve. It implies that the integrated electron energy goes as r^2 , i.e. most of the electron thermal energy is at the largest radii. For the Compton corona model we discuss in paper I, the bulk of the accretion and electron thermal energy is expected to be at radii $\lesssim 50 GM/c^2$.

5.4. Implications of the Coherence

The physical implications of the coherence function are discussed extensively in Vaughan & Nowak (1997). Here we point out some of the specific implications for Comptonization models. If the low frequency variability is reprocessed from the soft input photons, the near unity coherence between $\approx 0.02 - 10$ Hz indicates that on these timescales the Comptonizing medium must appear as a *static* medium. [As discussed by Nowak & Vaughan (1996), a static corona is a *linear* reprocessor.] If, on the other hand, the corona directly creates the low frequency variability, then it must do so in a global, linear fashion, despite the fairly large observed variability amplitudes.

As discussed by Vaughan & Nowak (1997), the loss of high frequency coherence is consistent with the presence of multiple, independent sources and responses. As the frequencies associated with the dynamical timescales are $\gtrsim 9$ Hz for $R \lesssim 50 GM/c^2$ and $M = 10 M_\odot$, the high frequency coherence loss and the “hardening” of the high frequency PSD with energy is consistent with the hypothesis that we are directly viewing the formation timescales and processes of the corona.

The loss of coherence below $\lesssim 0.02$ Hz is consistent with viscous timescales for $R \gtrsim 50 GM/c^2$. Perhaps on these low frequency timescales we are seeing the disk ‘global’ structure becoming disassociated from the corona ‘global’ structure.

We again note that although there seems to be a general trend for the coherence to drop for frequencies $\lesssim 0.02$ Hz, there apparently is a recovery at 0.005 Hz, coincident with the weak feature in the PSD. In general, we expect any global oscillation to be fairly coherent. The coherence associated with this feature makes it appear to be more significant than implied by the rather low 50–85% value suggested by a Lomb-Scargle periodogram (cf. §2). Unfortunately, we are not aware of any direct way of assessing the statistical significance of this coherence peak

coincident with the weak PSD feature.

6. SUMMARY

We have presented timing analysis for a 20 ks RXTE observation of Cygnus X-1, taken approximately two weeks after Cyg X-1 returned to its hard/low state from its soft/high state. It is possible that some of the properties of Cyg X-1 were slightly different from their “standard” hard/low state values (e.g. the 10–200 keV photon index). However, many of the timing properties were similar to previous observations (Miyamoto & Kitamoto 1989; Belloni & Hasinger 1990a; Belloni & Hasinger 1990b; Miyamoto et al. 1992).

We have presented detailed discussions of all the timing analyses used in this work, including discussions of errors and noise limits. We are very confident of our results for the PSD from 10^{-3} –100 Hz, for the coherence from 10^{-3} –30 Hz, and for the time delay from 0.1–30 Hz. The coherence function is the most sensitive to systematic errors (i.e., deadtime); however, the general trend of coherence loss out to ≈ 100 Hz is secure even with uncertainties as large as 25% in the deadtime. (*Ginga* systematic uncertainties were such that one could not be confident in coherence trends above ≈ 1 Hz; cf. Vaughan 1991; Vaughan & Nowak 1997.)

Some of the notable features of our observations were the 0.005 Hz feature and the high frequency ‘hardening’ with energy seen in the PSD. The former, if real, could be indicative of an oscillation on viscous timescales, whereas the latter may be indicative of dynamical timescale variability produced directly by the corona. The coherence function lends support to both of these interpretations. For the former, the coherence is seen to recover towards unity, whereas for the latter, the coherence is seen to drop in accord with theoretical expectations of multiple flaring regions (Vaughan & Nowak 1997). The coherence was also seen to be nearly unity from 0.02–10 Hz. Curiously, the 0.01–0.2 Hz coherence between the lowest and highest energy bands was seen to be slightly greater than the coherence between the lowest and second highest energy bands.

We also made comparisons of our timing analysis to the expectations of simple Comptonization models. The high frequency PSD in the highest energy channels was *not* as attenuated as expected for simple corona models, again lending credence to the hypothesis that we are seeing direct modulation by a fluctuating corona. Although the time lags show the expected logarithmic dependence upon energy, their increase with decreasing Fourier frequency is contrary to the simplest expectations for a relatively compact, uniform corona. We explore this point further in a companion paper (paper III).

Both our energy spectral analysis of paper I and the timing analysis presented here show that the simplest models are inadequate for describing the high quality RXTE data. Due to its broad spectral coverage, RXTE allows us to compare and discriminate among detailed, self-consistent models for the energy spectrum. Coupling these detailed models (as we do in paper III) with RXTE’s superior timing capabilities places further constraints on their structure, and more importantly, on their dynamics. Only those models in which *both* the spectral and temporal data can be explained should be considered valid candidates for Cygnus X-1.

We would like to acknowledge useful discussions with P. Michelson, E. Morgan, K. Pottschmidt, R. Staubert, M. van der Klis, and W. Zhang. This work has been financed by NSF grants AST91-20599, AST95-29175, INT95-13899, NASA Grants

NAG5-2026, NAG5-3225, NAGS-3310, DARA grant 50 OR

92054, and by a travel grant to J.W. from the DAAD.

REFERENCES

Aab, O. É., Bychkova, L. V., Kopylov, I. M., & Kumařgorodskaya, R. N., 1984, Sov. Astron., 28, 90 (orig.: AZh, 61, 152, 1984)

Angelini, L., & White, N. E., 1992, IAU Circ. 5580

Angelini, L., White, N. E., & Stella, L., 1994, in *New Horizon of X-Ray Astronomy*, ed. F. Makino, T. Ohashi, (Tokyo: Universal Academy Press), 429

Batucińska-Church, M., Belloni, T., Church, M. J., & Hasinger, G., 1995, A&A, 302, L5

Balog, N. I., Goncharskii, A. V., & Cherepashchuk, A. M., 1981, Sov. Astron. Lett., 7, 336 (orig.: Pis'ma Astron. Zh., 7, 605, 1981)

Belloni, T., & Hasinger, G., 1990a, A&A, 227, L33

Belloni, T., & Hasinger, G., 1990b, A&A, 230, 230

Bendat, J., & Piersol, A., 1986, *Random Data: Analysis and Measurement Procedures*, (New York: Wiley)

Bochkarev, N. G., Karitskaya, E. A., Luskutov, V. M., & Sokolov, V. V., 1986, Sov. Astron., 30, 43 (orig.: AZh, 63, 71, 1986)

Bowyer, S., Byram, E. T., Chubb, T. A., & Friedman, H., 1965, Science, 147, 394

Brainerd, J., & Lamb, F. K., 1987, ApJ, 317, L33

Bussard, R. W., Weisskopf, M. C., Elsner, R. F., & Shibasaki, N., 1988, ApJ, 327, 284

Coppi, P. S., 1992, MNRAS, 258, 657

Crary, D. J., Finger, M. H., van der Hooft, C. K. F., van Paradijs, J., van der Klis, M., & Lewin, W. H. G., 1998, ApJ, submitted

Cui, W., Heindl, W. A., Rothschild, R. E., Zhang, S. N., Jahoda, K., & Focke, W., 1997a, ApJ, 474, L57

Cui, W., Zhang, S. N., Focke, W., & Swank, J. H., 1997b, ApJ, 484, 383

Dolan, J. F., 1992, ApJ, 384, 249

Dove, J. B., Wilms, J., & Begelman, M. C., 1997, ApJ, 487, 747

Dove, J. B., Wilms, J., Maisack, M. G., & Begelman, M. C., 1997, ApJ, 487, 759

Dove, J. B., Wilms, J., Nowak, M. A., Vaughan, B. A., & Begelman, M. C., 1998, MNRAS, in press (paper I)

ESA, (eds.) 1997, *The Hipparcos and Tycho Catalogues*, ESA SP 1200, (Noordwijk: ESA Publications Division)

Gierliński, M., Zdziarski, A. A., Done, C., Johnson, W. N., Ebisawa, K., Ueda, Y., Haardt, F., & Phlips, B. F., 1997, MNRAS, in press

Gies, D. R., & Bolton, C. T., 1982, ApJ, 260, 240

Gies, D. R., & Bolton, C. T., 1986, ApJ, 304, 304

Haardt, F., & Maraschi, L., 1993, ApJ, 413, 507

Herrero, A., Kudritzki, R. P., Gabler, R., Vilchez, J. M., & Gabler, A., 1995, A&A, 297, 556

Hjellming, R. M., 1973, ApJ, 182, L29

Hua, X.-M., & Titarchuk, L., 1995, ApJ, 449, 188

Hutchings, J. B., 1978, ApJ, 226, 264

Jahoda, K., Swank, J. H., Giles, A. B., Stark, M. J., Strohmayer, T., Zhang, W., & Morgan, E. H., 1996, in *EUV, X-Ray, and Gamma-Ray Instrumentation for Astronomy VII*, ed. O. H. Siegmund, (Bellingham, WA: SPIE), 59

Kazanas, D., Hua, X.-M., & Titarchuk, L., 1997, ApJ, 480, 280

Kouveliotou, C., Finger, M. H., Fishman, G. J., Meegan, C. A., Wilson, R. B., & Paciesas, W. S., 1992, IAU Circ. 5576

Kylafis, N. D., & Klimis, G. S., 1987, ApJ, 323, 678

Kylafis, N. D., & Phinney, E. S., 1989, in Ögelman & van den Heuvel 1989, 731

Leahy, D. A., Darbro, W., Elsner, R. F., Weisskopf, M. C., Sutherland, P. G., Kahn, S., & Grindlay, J., 1983, ApJ, 266, 160

Liang, E. P., & Nolan, P. L., 1984, Space Sci. Rev., 38, 353

Lomb, N. R., 1976, Ap&SS, 39, 447

Lutz, J. H., & Lutz, T. E., 1972, AJ, 77, 376

Miller, G. S., & Lamb, F. K., 1992, ApJ, 388, 541

Miller, M. C., 1995, ApJ, 441, 770

Miyamoto, S., Kimura, K., Kitamoto, S., Dotani, T., & Ebisawa, K., 1991, ApJ, 383, 784

Miyamoto, S., & Kitamoto, S., 1989, Nature, 342, 773

Miyamoto, S., Kitamoto, S., Iga, S., Negoro, H., & Terada, K., 1992, ApJ, 391, L21

Morgan, E. H., Remillard, R. A., & Greiner, J., 1997, ApJ, 482, 993

Narayan, R., 1996, ApJ, 462, 136

NASA, 1997, *Rossi X-ray Timing Explorer Guest Observer Program, Cycle 3*, Technical Report NRA 97-OSS-09, (Washington, DC: NASA Office of Space Science)

Ninkov, Z., Walker, G. A. H., & Yang, S., 1987a, ApJ, 321, 438

Ninkov, Z., Walker, G. A. H., & Yang, S., 1987b, ApJ, 321, 425

Nowak, M. A., & Vaughan, B. A., 1996, MNRAS, 280, 227

Nowak, M. A., Wilms, J., Vaughan, B. A., Dove, J., & Begelman, M. C., 1998, ApJ, submitted (paper III)

Oda, M., 1977, Space Sci. Rev., 20, 757

Ögelman, H., & van den Heuvel, E. P. J., (eds.) 1989, *Timing Neutron Stars*, NATO ASI C262, (Dordrecht: Kluwer)

Pottschmidt, K., 1997, Diplomarbeit, Eberhard-Karls-Universität, Tübingen

Pottschmidt, K., König, M., Wilms, J., & Staubert, R., 1998, A&A, in press

Poutanen, J., Krolik, J. H., & Ryde, F., 1997, MNRAS, 221, 21p

Poutanen, J., Svensson, R., & Stern, B., 1997, in Winkler, Courvoisier & Durouchoux 1997, 401

Pozdnyakov, L. A., Sobol, I. M., & Sunyaev, R. A., 1983, 2, 189

Scargle, J. D., 1982, ApJ, 263, 835

Shakura, N. I., & Sunyaev, R., 1973, A&A, 24, 337

Shakura, N. I., & Sunyaev, R. A., 1976, MNRAS, 175, 613

Sokolov, V. V., 1987, Sov. Astron., 31, 419 (orig.: AZh, 64, 64, 1987)

Stollman, G. M., Hasinger, G., Lewin, W. H. G., van der Klis, M., & van Paradijs, J., 1987, MNRAS, 227, 7p

Sunyaev, R. A., & Titarchuk, L. G., 1980, A&A, 86, 121

Sunyaev, R. A., & Trümper, J., 1979, Nature, 279, 506

Svensson, R., & Zdziarski, A. A., 1994, ApJ, 436, 599

Tanaka, Y., & Lewin, W. H. G., 1995, in *X-Ray Binaries*, ed. W. H. G. Lewin, J. van Paradijs, E. P. J. van den Heuvel, (Cambridge), Chapt. 3, 126

Turon, C., Crézé, M., Egret, D., Gómez, A., et al., 1992, *The Hipparcos Input Catalogue*, ESA-SP 1136, (Noordwijk: ESA Publications Division)

Ubertini, P., Bazzano, A., Cochhi, M., La Pudla, C., Polcaro, V. F., Staubert, R., & Kendziorra, E., 1994, ApJ, 421, 269

van der Klis, M., 1989, in Ögelman & van den Heuvel 1989, 27

Vaughan, B. A., 1991, Dissertation, Stanford University, Stanford, CA

Vaughan, B. A., & Nowak, M. A., 1997, ApJ, 474, L43

Vikhlinin, A., et al., 1994, ApJ, 424, 395

Walborn, N. R., 1973, ApJ, 179, L123

Wijers, R. A. M. J., van Paradijs, J., & Lewin, W. H. G., 1987, MNRAS, 228, 17p

Wilms, J., Dove, J., Staubert, R., & Begelman, M. C., 1997, in Winkler, Courvoisier & Durouchoux 1997, 233

Winkler, C., Courvoisier, T. J.-L., & Durouchoux, P., (eds.) 1997, *The Transparent Universe*, ESA SP 382, (Noordwijk: ESA Publications Division)

Wu, C.-C., Eaton, J. A., Holm, A. V., Milgrom, M., & Hammerschlag-Hensberge, G., 1982, PASP, 94, 149

Zhang, S. N., Cui, W., Harmon, B. A., Paciesas, W. S., Remillard, R. E., & van Paradijs, J., 1997, ApJ, in press

Zhang, W., & Jahoda, K., 1996, *Deadtime Effects in the PCA*, Technical report, (Greenbelt: NASA GSFC), version dated 1996 September 26

Zhang, W., Jahoda, K., Swank, J. H., Morgan, E. H., & Giles, A. B., 1995, ApJ, 449, 930